Norwegian University of Science and Technology - NTNU
Faculty of Physics, Informatics and Mathematics
Department of Physics

DIPLOMA THESIS

FOR

STUD.TECHN. Tommy Nakken Aalerud

FACULTY OF PHYSICS, INFORMATICS AND MATHEMATICS
NTNU

Thesis started: October 1, 2000
Thesis to be delivered by: February 15, 2001
Delivery date extended to: March 1, 2001
Thesis delivered: March 1, 2001

DISCIPLINE: MATERIAL AND SOLID STATE PHYSICS

Norwegian title: "Synkrotron røntgenspredningsstudier av vanninterkalering i syntetisk nikkel-fluorohektonitt"
English title: "Synchrotron X-ray Scattering Studies of Water Intercalation in Synthetic Nickel-Fluorohectorite"
Purpose of the work:
Studies of prepared pressed synthetic smectite clays by means of synchrotron X-ray scattering, investigating bulk and surface water transport properties.

This work is to be carried out at Department of Physics, NTNU, under the supervision of Jon Otto Fossum.

Trondheim, March 1, 2001

Supervisor
Associate Professor Dr.ing. Jon Otto Fossum
Department of Physics

ACKNOWLEDGEMENTS

The work with the diploma thesis has been performed at the Group of Material Science and Solid State Physics, Department of Physics at the Norwegian University of Science and Technology (NUST) in Trondheim. From October 24th to November 7th X-ray experiments were done at Brookhaven National Laboratory, Upton, New York. These two weeks working at a real synchrotron lab gave a good insight into how real scientists work. The trip to the USA was a cultural experience as well.

First of all I have to thank my supervisor, Jon Otto Fossum, who has made it possible to do this diploma thesis. His contribution with ideas and hints has been important in my work. I would also like to thank Geraldo Jose da Silva whom I have co-operated with in analysing the data, as well as Kenneth Dahl Knudsen who was together with me and dr. Fossum the last week at BNL. The Physics Workshop has been of great importance because they have made the clay-press, and Arnolf Bjølstad has been helpful in contributing with ideas to the design of the press. Finally I would like to thank my office-mate and co-worker Magnus Willum Haakestad for his help on the lab, motivation through the writing of the diploma thesis and explicit help with details in the text.

Trondheim, March 1st, 2001

Tommy N. Aalerud

SUMMARY

This diploma thesis is primarily an experimental X-ray scattering study of Ni-fluorohectonite, a synthetic smectite clay. Analysis of the peak positions in θ - 2θ scans for the 001 Bragg peak for the 0, 1, 2 and 3 water layer situations in this clay has shown that the distance between the clay sheets is linearly dependent of the number of intercalated water layers. When an additional water layer is intercalated, the distance increases with about 2.3 Å, or equivalent to the size of a water molecule. The number of sheets in each crystal corresponding to the crystal size, N, has also been investigated. The most likely value of this N is around 100, and it might be dependent of the amount of water intercalated giving a larger value for the three-water-layer situation. From an analysis of the amount of randomness of the crystal organisation, the sample is found to behave much like a random powder.

A clay press and a procedure for drying clay sample under high pressure were developed. The procedure has successfully made samples of Na-fluorohectorite using a pressure of 10 tons.

INTRODUCTION

Motivation

Clay minerals are hydrous aluminum silicates and are classified as phyllosilicates or layer silicates. Within the family called clays there is considerable variation in chemical and physical properties. Because clay minerals usually are less than 2 microns in size, the particles are too small to be studied by optical or single crystal X-ray methods. Historically the structural and chemical details of these minerals have been extrapolated from X-ray studies of their macroscopic counterparts. The use of X-ray diffraction techniques the last two decades has made it possible for us to gain information about the clay structures from the electrons surrounding the atoms that make-up the clay crystals.

The goal for this diploma thesis was to investigate X-ray dynamics in synthetic smectite Na-fluorohectorite. Earlier synchrotron experiments on clays have been performed on surface scattering samples, but using this type of experiments on bulk samples has not been done before.

The diploma work

The report summarises experimental work on preparing clay samples of Na-fluorohectorite as well as X-ray diffraction studies of Ni-fluorohectorite. The original idea when the diploma work started was to prepare Na-fluorohectorite samples at a higher pressure than earlier and study them to find out if the clay crystals were better aligned than in the previous samples. It turned out to be more difficult and took more time than expected to prepare the new clay samples. We did not have time to make any new samples before the X-ray experiments started, so we had to use some old samples made at a much lower pressure with a different interlayer cation. After the X-ray experiments were finished, the process of preparing clay samples was continued while the X-ray data was analysed and the diploma thesis written.

1 THEORY

1.1 Diffraction

There are two different widely used techniques to reveal the atomic structure, size and dynamics of colloidal systems. They are X-ray scattering and neutron scattering. The major difference is that X-rays are scattered by electrons in the material while neutrons are scattered by the nuclei. I have used X-ray scattering, and the following pages explain how such scattering patterns occur and how they can be explained. The presentation is based on an introduction book in molecular biophysics [7] and a textbook about X-ray diffraction procedures [8]. Some inspiration has also come from the book *X-ray Diffraction and the Identification and Analysis of Clay Minerals* [9].

Diffraction is a familiar phenomenon to us all. When we see the beautiful rainbow on the surface of a compact disc, the sparkling colours from a drop of oil on water or from the wings of a butterfly, these effects are dependent on the properties of light and are caused by diffraction. The essential for diffraction is that the distance between the scattering centres must be about the same as the wavelength of the waves being scattered. The reason why X-rays have been used in this study is that the wavelength of X-rays and the spacing between the crystals meet this condition, both have a dimension of about 1 Å or 0.1 nm.

1.1.1 Scattering

When we are performing our diffraction studies we benefit from the wave-like property of photons. Like all electromagnetic radiation X-rays can be characterised in terms of a single, polarised ray with an electric vector **E** vibrating perpendicular to the direction of propagation and a magnetic vector **H** perpendicular to both the electric vector and the direction of propagation. The electric vector is interesting to us because when an incident ray encounters an electron, the electron will vibrate with the same frequency as the incoming electric vector field. The electron absorbs a small amount of energy from the incident beam, and reradiates this energy with the same wavelength in all directions due to its vibration. The phenomenon is called **coherent scattering**. When photons are scattered against atoms in a material, some small amount of the incident particles' linear momentum is transferred to the atoms. In our case, however, this loss in energy is in fact so small that we consider the energy and thereby the wavelength to be conserved.

The scattering power f of an atom increases with the number of electrons bound to the atom. The value of f is somewhat smaller than the atomic number multiplied with the scattering power of a single electron. This is because the outgoing waves from different electrons belonging to the same atom will be slightly out of phase with each other, resulting in destructive interference.

1.1.2 Bragg's Law

When we use a diffractometer to study clay minerals we need to visualise what is referred to as the reflection of X-rays. The alternative experimental mode is when the X-ray beam penetrates the sample and the intensity is detected on the opposite side of the incoming ray. But when we have reflection of X-rays the situation is like figure 1.1 below.

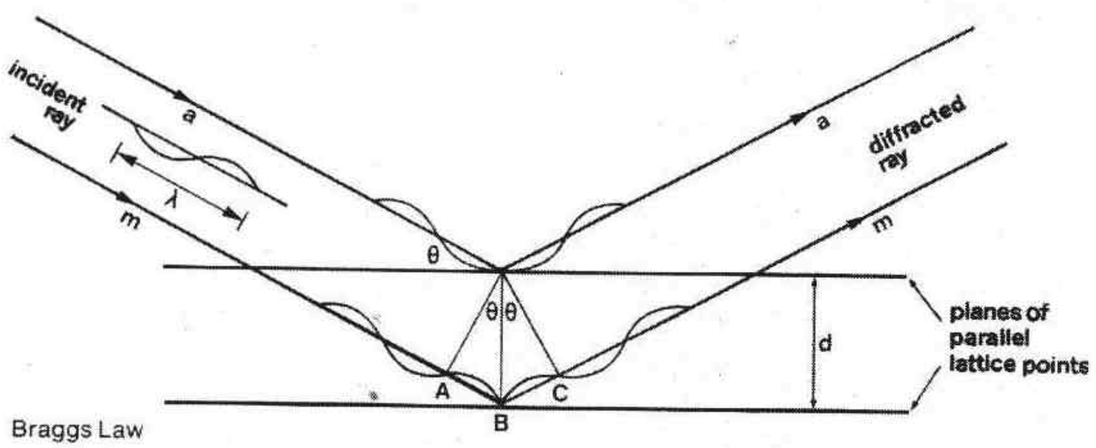

Figure 1.1. Diffraction from two parallel planes illustrating Bragg's law. The figure is taken from a Siemens poster.

From the figure we can see that the path difference between the two reflected rays is AB + BC = 2d sin θ. When the path difference is an integer number of whole wavelengths, a distinct peak in the measured intensity will be observed. This is the essence of Bragg's law. Figure 1.2 defines the scattering vector **q**.

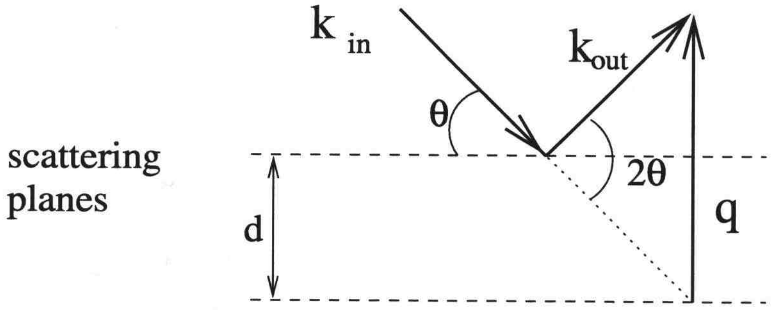

Figure 1.2. The definition of **q** for X-ray reflection.

With the definition of **q** we can easily deduce the following equalities when this definition is substituted into Bragg's law.

$$q = |\mathbf{q}| = 2k\sin q = \frac{4p}{l}\sin q \tag{1.1}$$

$$d = \frac{2pn}{q} \tag{1.2}$$

In the last equation n is the path difference between the interfering rays. From equation (1.2) we see that the position of the 001 peak (n=1) directly will give us d, the spacing in our clay structure.

Some simplifying assumptions were made to derive the Bragg equation, as always when we try to model nature. For this equation to be correct the incident beam must be perfectly monochromatic and the incoming rays perfectly parallel. Of additional importance is that the equation is based on having only three rows of perfectly ordered atoms in a perfect and infinite crystal perfectly oriented for diffraction to occur. But our real circumstances are not so ideal. We need to include some important factors in our data analysis.

1.1..3 Information from Intensity

Much and thorough work has been done to understand the diffraction patterns from clay systems. Detailed theory for such analysis can be found in the X-ray diffraction book of Moore and Reynolds Jr. [9]. When we analyse our clay samples, the information about them is found from the positions of the peaks and their shapes. For example the peaks get sharper when the crystals get thicker and contain more scattering planes. For our clay samples the crystal size is small, the crystals are not perfect and our peaks get broader.

The contribution to the total scattered intensity comes from the interference function, $\Phi(\theta)$, the layer scattering factor, $G(\theta)$, and the Lorenz polarisation factor, $Lp(\theta)$. The interference function contributes to evenly spaced peaks of the same intensity giving us the positions of the different Bragg peaks. The layer scattering intensity, which is the square of the scattering factor, gives different intensities for different angles because of the scattering factors and the placements of the divers atoms that are represented. The Lorenz polarisation factor models that the degree of polarisation of the beam in the sample is related to the angle and also the difference in the volume exposed to primary irradiation as well as the number of crystals favourably oriented for diffraction.

1.1.4 The interference function, Φ

The interference function is a continuous function and is given by

$$\Phi(\theta) = \frac{\sin^2(2\pi ND\sin\theta / \lambda)}{\sin^2(2\pi D\sin\theta / \lambda)} \tag{1.3}$$

where N is the thickness of the crystal in number of unit cells along the Z axis and D is the d spacing. The calculation of the interference function assumes that the d spacing is uniform in every crystallite. Figure 1.3 shows how the interference function looks like with N=15 and d=10 Å.

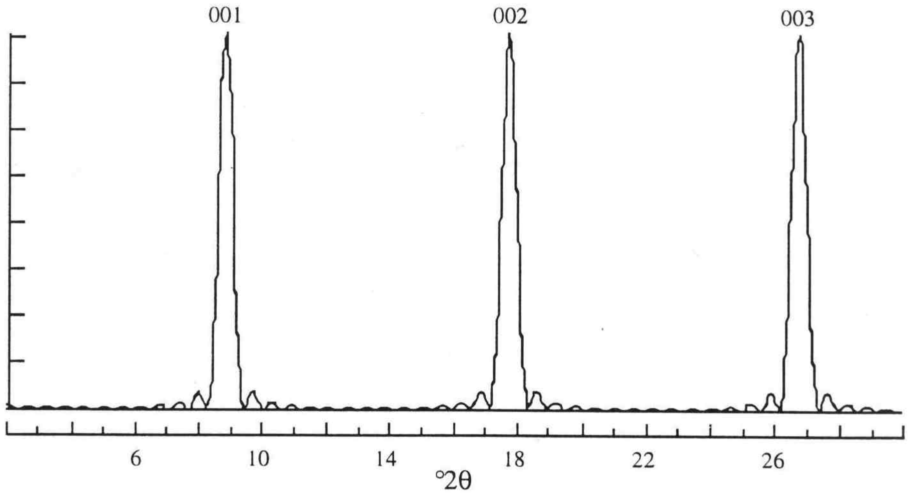

Figure 1.3. Interference function (Φ) for N=15 and d=10 Å, taken from [9].

On this figure there are clearly visible ripples in the background. Such ripples are not natural and they do not occur in real scans, but in our model they're there because we have assumed that diffraction occurs only from crystals made up of exactly N=15 unit cells. A better way to model the interference function is if we assume that the array causing the diffraction is made up of crystals with different values for N. If q(N) is the proportion of crystallites of thickness N, normalised to 1, we divide our interference function by N and get the following equation.

$$\Phi(q) = \sum_{N=n_1}^{N=n_2} \frac{\sin^2(2pND\sin q / l)}{N\sin^2(2pD\sin q / l)} \tag{1.4}$$

The result of this equation is seen in figure 1.4.

1.1.5 The layer scattering factor, G

The layer scattering factor represents the scattering efficiency of a unit cell and is given by:

$$G(q) = \sum_n P_n f_n \cos(\frac{4pz_n \sin q}{l}) \tag{1.5}$$

In the equation P_n represents the number of atoms of type n, f_n is their scattering power and z_n is the displacement in Å from the centre of symmetry. The measured scattering intensity is the squared of G(θ). Figure 1.4 shows a typical example of how the layer scattering intensity will look like as a function of the angle.

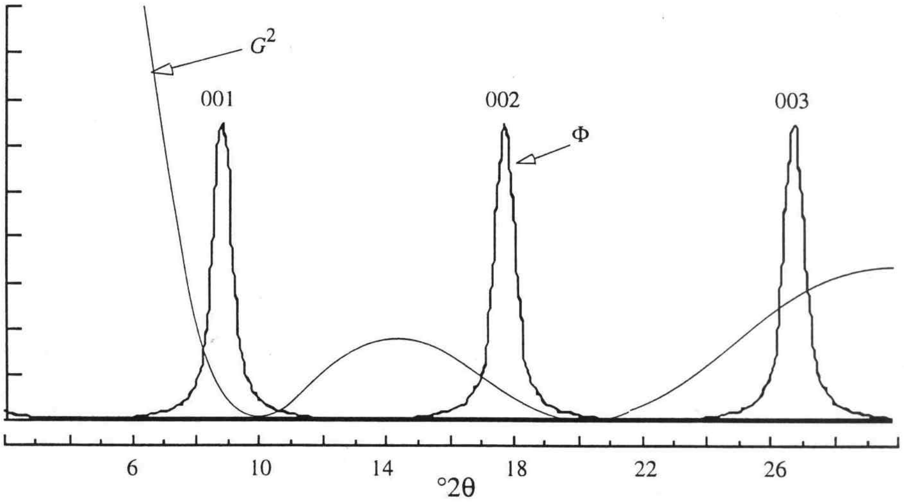

Figure 1.4. Interference function with N from 2 to 15, d=10 Å and $G^2(\theta)$ for a unit cell. Figure is taken from [9].

The layer scattering intensity has local minima and maxima which can make some of the Bragg peaks invisible while others, especially the 001 peak, get large.

1.1.6 The Lorenz-Polarisation Factors, Lp

The Lorenz-polarisation factors are a combination of two factors. The polarisation factor increases the values of the peaks and the background from a maximum at low angles to a minimum at high angles. The reason for this change is that as radiation comes from the synchrotron it is unpolarised, but the scattering cases a degree of polarisation dependent on the angle of the incident and diffracted beams. The X-rays get polarised as they are diffracted from a plane of atoms in the same way light is polarised by reflecting off the hood of a car. The energy of the scattered beam is proportional to the polarisation factor, $(1+\cos^2(2\theta))/2$, where θ is the angle between the incident beam and the reflecting surface.

The Lorenz factor is actually a combination of two factors. The first handles the volume of the increment of the crystal that is exposed to primary irradiation, and the second relates the number of crystals favourably oriented for diffraction at Bragg angle θ. For a single crystal the Lorenz-polarisation factors are

$$Lp = \frac{1+\cos^2 2q}{\sin 2q \sin^n q} \tag{1.6}$$

with n=0. For random powders n=1. For our clay samples the value of n is assumed to be between 0 and 1.

Figure 1.5 shows an example of the Lorenz-polarisation factor.

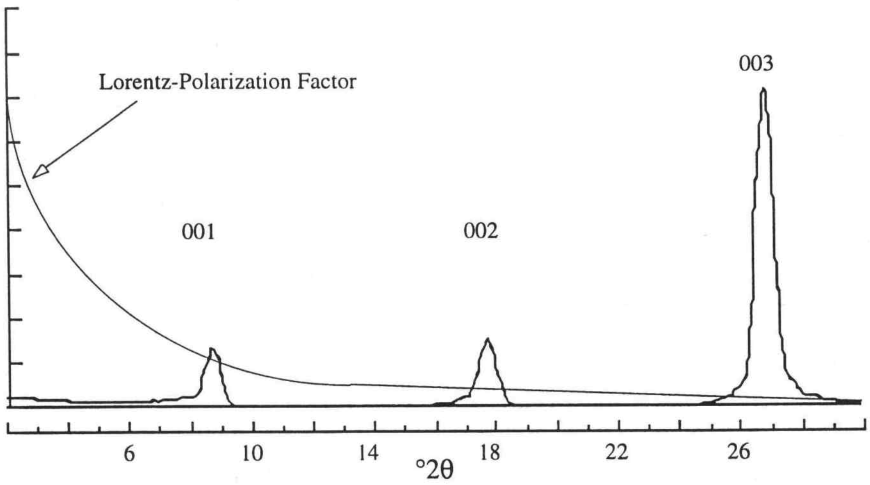

Figure 1.5. The Lorenz-polarisation factor and the product of G^2 and Φ, taken from [9].

1.1.7 Putting it all together

The total intensity is calculated by taking the products of Φ, G^2 and Lp.

$$I(q) = \left[G^2(q)\right]\left[\Phi(q)\right]\left[L_p(q)\right] \tag{1.7}$$

The figure in appendix f shows how the total modelled intensity pattern will look like.

1.2 Williamson-Hall Analysis

In a well known X-ray article from Williamson and Hall concerning an analysis of the X-ray line broadening from filed aluminium and wolfram [10], it is suggested that the observed effect of line broadening can be attributed to simultaneous small particle size and strain broadening. The result given in this article is that the breadth, or the FWHM, measured in radians is a linear function of tan θ.

In general the breadth β is approximated by

$$b = 2x \tan q + \frac{l}{t \cos q} \tag{1.8}$$

and in this equation λ is the wavelength. The first term comes from the limit of resolution and is obtained by differentiating Bragg's law, and the second term is the Scherrer equation which relates the broadening of an X-ray beam to the crystal size t. For more details see [11]. We have the relation

$$q = \frac{4p}{l}\sin q \tag{1.9}$$

and we can write the breadth in q, Δq, as

$$\Delta q = \frac{4p}{l}\cos q \cdot \Delta q \tag{1.10}$$

Replacing Δθ with β and inserting (1.8) into (1.10) gives

$$\frac{l}{4p}\Delta q = 2x\sin q + \frac{l}{t} \tag{1.11}$$

when multiplying with λ/4π. In equation (1.11) the t is the crystal size and is the same as Nd or the number of sheets in each crystal times the distance between them. When we plot

$$y = w \cdot \cos q = \frac{l}{4p} \cdot w \tag{1.12}$$

as a function of

$$x = \sin q = \frac{l}{4p} \cdot x_c \tag{1.13}$$

the intercept will be λ/Nd. The d is 2π/q_c where q_c is the q-position of the 001 peak. Here ω is the peak width in $Å^{-1}$ and x_c is the centre position of the peak. If we call the intercept A we get this expression for N which is the number of sheets or the crystal's size.

$$N = \frac{l}{2p} \cdot \frac{q_c}{A} \tag{1.14}$$

2 CLAYS

2.1 Clay minerals

Natural clay minerals are the smallest physical structures in geology. Initially, clays were defined as consisting of grains smaller than 2μm in diameter. This was the definition of the 19th century, because of the microscopic limit. On figure 2.1 Wentworth's scale is shown. It is commonly used in North America, and it gives names to the different structures in geology based on their size.

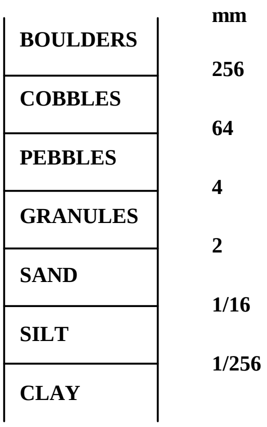

Figure 2.1. Wentworth's scale. [1]

The different types of clays have a similar mineral structure in addition to their common grain size; most of them have a sheet structure. Both natural clays and synthetically made clays have these sheet structures.

The most important property of some clay minerals is the swelling property, the capacity to change volume by absorbing water molecules or other polar liquids into the structure. Such swelling clays are called **smectites**. There are many different types of swelling and non-swelling clays, but I will focus on fluorohectorite, a strong swelling clay. For a complete introduction to different types of clays, their structure and chemical composition, the works of B. Velde [1] and H. van Olphen [2] can be recommended.

2.2 Phase diagram

An important part of this diploma thesis has been the making of clay dispersions when mixing clay powder and distilled water and adding interlayer cations from added salt. Then the water is dried out again under pressure. Figure 2.2 shows the phase diagram for montmorillonite, a smectite clay. But for the discussion of the phase diagram that follows, it is not important, because the phase diagram for fluorohectorite is built by the same principles, even though we do not know exactly how it looks like.

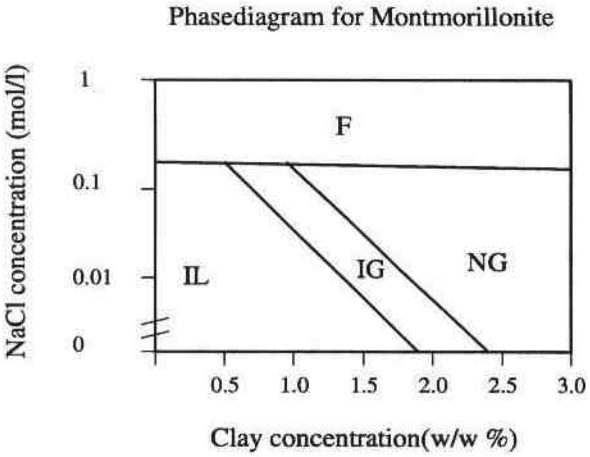

Figure 2.2. Phasediagram for montmorillonite. Taken from [3].

In this diagram we start in the bottom left corner, and the solution is characterised as an isotropic liquid (IL). When the concentration of clay is increased, we move to the right eventually crossing into the isotropic gel (IG) and nematic gel (NG) phases. When the salt is added, we move upwards in the diagram and into the state of flocculation (F). Here the clay particles coagulate, and there will be a clear phase above.

2.3 Clay crystal structure

Clay minerals are classified as phyllosilicates or layer silicates. In the sheet structure of clays there are three fundamental molecular units: A tetrahedron, an octahedral polyhedron and an interlayer cation. The tetrahedron shown in figure 2.3 consists of four oxygen anion with one cation in the centre. The dominant cation is Si^{4+}, but Al^{3+} substitutes frequently and Fe^{3+} occasionally.

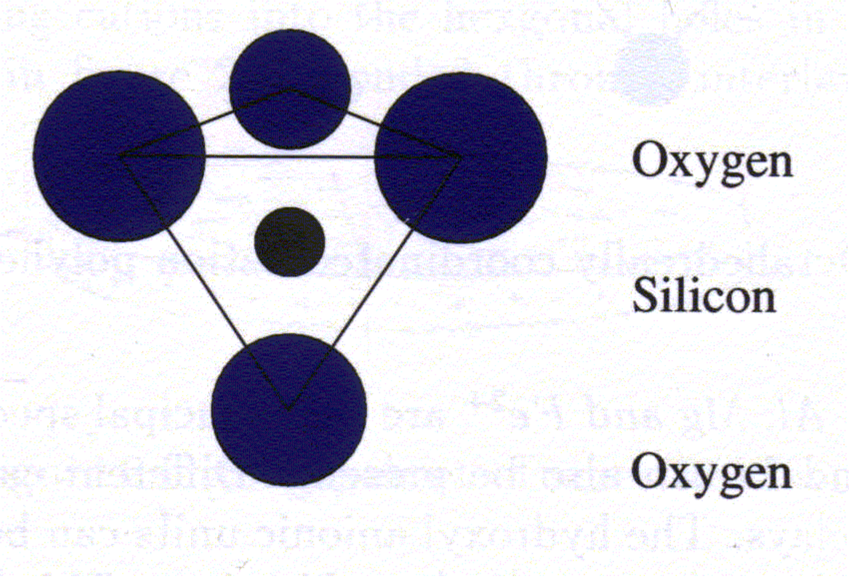

Figure 2.3. Tetrahedron, the basic unit of the clay structure. Taken from [16].

The tetrahedra are linked to each other by highly covalent bonding through the sharing of oxygen atoms. The tetrahedral sheets can be pictured as extending infinitely in two dimensions. Each tetrahedron rests on a triangular face and shares the oxygens at all three corners, the basal oxygens, with three other tetrahedra. The fourth oxygen, called the apical oxygen, is shared with the octahedral sheet.

The octahedral sheet can be thought of as two planes of closest-packed oxygen ions with cations occupying the resulting octahedral sites between the two planes. Figure 2.4 shows the octahedrally coordinated cation polyhedron. The octahedral cations are coordinated with six oxygens or hydroxyl units.

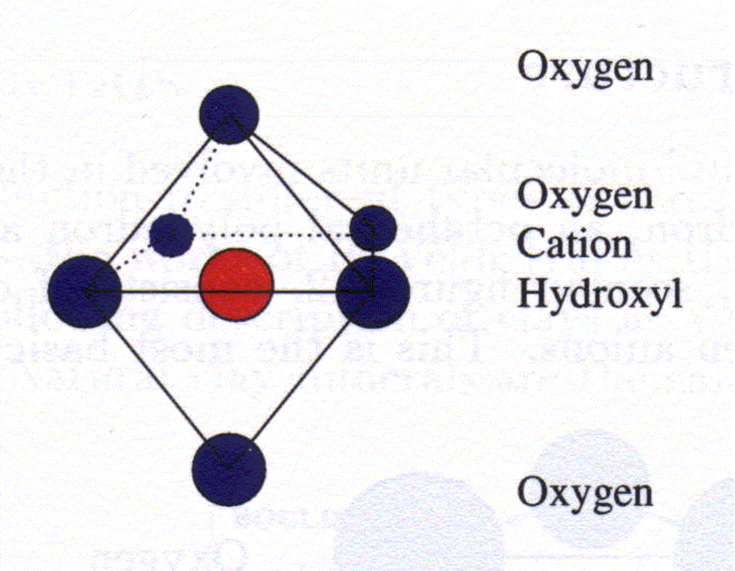

Figure 2.4. The octahedrally coordinated cation polyhedron. Taken from [16].

Sharing of neighbouring oxygen ions forms a sheet of edge-linked octrahedra extending infinitely in two dimensions. The octahedral cations are usually Al^{3+}, Mg^{2+}, Fe^{2+} or Fe^{3+}, but other transition elements as well as Li have been identified. Different cations give different names to the clay. In some of the clay structures the hydroxyl units can be replaced to some extent by F or Cl anions. For the fluorohectorite all hydroxyl groups have been replaced with fluorine.

The octahedrally coordinated layer is sandwiched between two tetrahedral sheets. This arrangement is called a 2:1 structure. Fluorohectorite is called a trioctahedral smectite, and this means that all of the three possible sites in the octahedrally coordinated layer are filled. Figure 2.5 shows the structure of fluorohectorite.

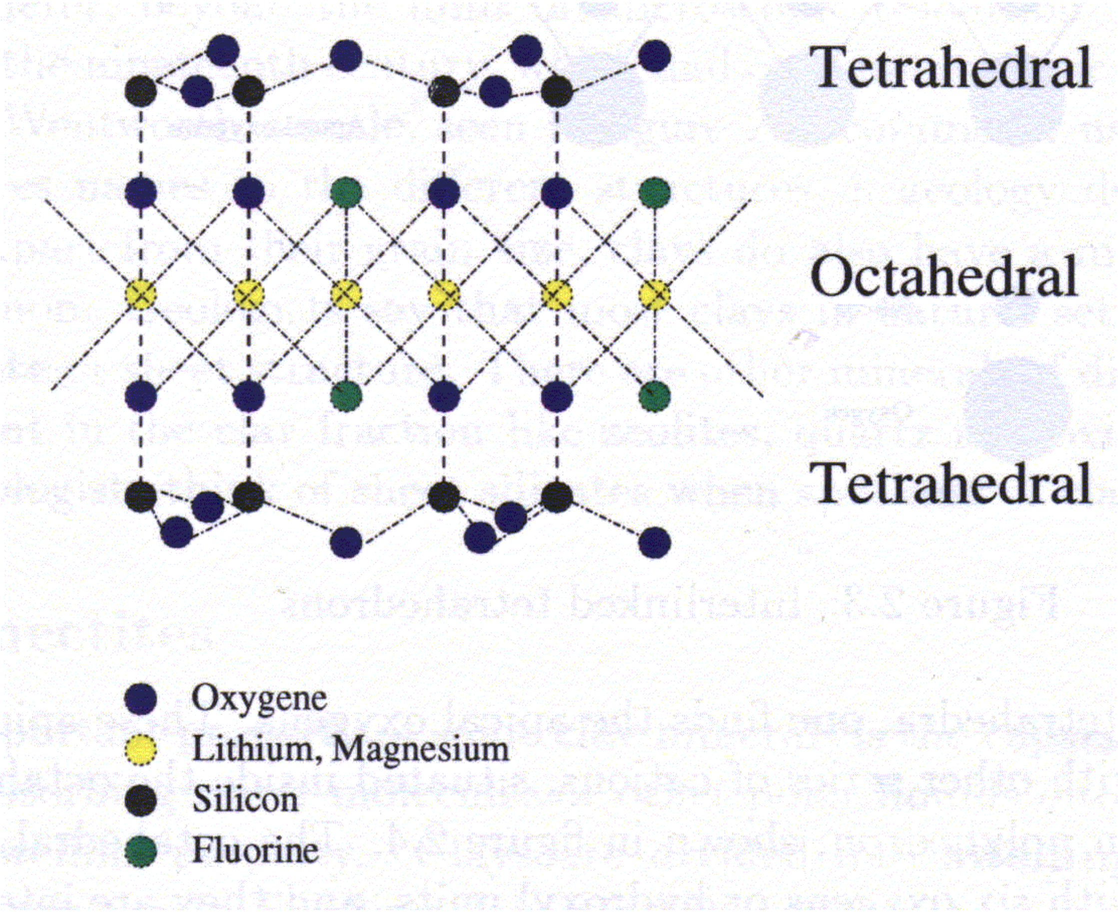

Figure 2.5. The structure of fluorohectorite. Taken from [16].

2.4 Interlayer cation

The layer charge in fluorohectorite originates from Li$^+$ substituting for Mg^{2+} in the octahedral layer [4], and the charge is 0.6e$^-$ pr. Si_4O_{10} unit. Fluorohectorite has also particle size of up to about 20000 Å, and this synthetic hectorite is an extreme both in particle size and layer charge.

Cation substitution in the sheet structure creates a negative surface charge on the sheets. This charge imbalance is compensated by loosely bounded cations between the layers. Figure 2.7 shows a 3D-drawing of a smectite. The distance between the sheets in figure 2.7 is called the **d-spacing**. The distance is dependent on how the interlayer cations are organised between the sheets and if there are any molecules like water intercalated in the structure.

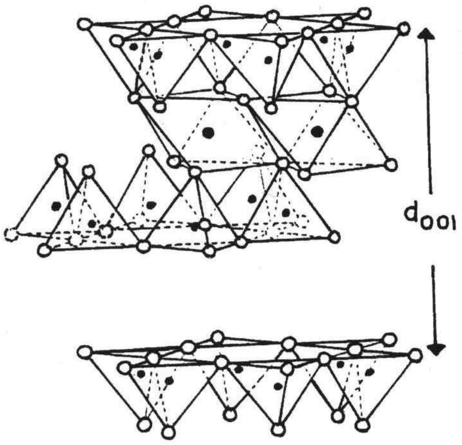

Figure 2.7. 3D-figure of a smectite. Taken from Solin & Lee [5].

2.5 Interlayer cation exchange

The swelling process is observed when smectites are immersed in an aqueous solution as a result of a mixture of different forces between the charged clay platelets and the influence of chemical equilibrium in the solution [6]. When water intercalates between the sheets, the surface charge can no longer keep the cations in place and they can be replaced. By adding a proper amount of salt to this water, it is possible to exchange the original interlayer cations with the cations from the salt. This can be done to study clays with different interlayer cations.

3 EXPERIMENTS

3.1 Clay-press

The idea of drying clay samples under pressure is that it might give samples that are better aligned. A rocking scan of such samples would give a narrower peak indicating that the orientational distribution of the crystal fragments is more homogenous. We know that the properties of clay in formations at the bottom of the sea are dependent on the pressure, and we wanted to find the pressure needed to reduce the pore size in the micro-pores in the clay.

Previous samples were made using a load of 500 N giving a pressure of 120 kPa. We wanted to model the pressure 5000 m under the sea level, where the pressure is about 7500 psi or 51700 kPa and the temperature is 130 °C. With this kind of pressure we had to design a new press.

With an internal diameter of 70 mm, 21000 kg is needed to give the pressure we wanted. The design of the new press was based on the old press but reinforced to cope with the higher pressure.

Figure 3.1. Outer cylinder with temperature element mounted

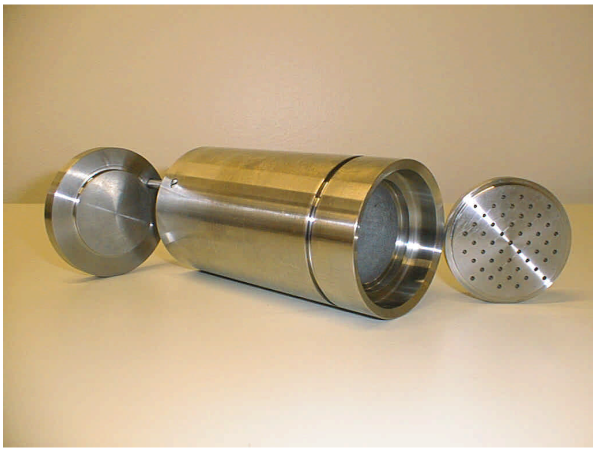

Figure 3.2. The inner cylinder.

In figures 3.1 and 3.2 above the new press is shown. Appendix A has more details about the design of the new press. The basic idea of the clay-press is two cylinders, one inside the other. The gap between is as small as possible, but large enough for the cylinders to slide. At the lower end of the inner cylinder an o-ring is placed to prohibit the liquid to pass and leak out when the pressure increases. The clay-liquid is filtered through a glass filter lying against a metal plate with several holes in it. The glass filter is covered with a paper filter to prohibit the clay to stick to it.

3.2 Sample preparation

We wanted to make samples of sodium fluorohectorite. A synthetic fluorohectorite purchased from Corning Inc. US was used, and we had to add the sodium ions. It is best to work with synthetic clay like this, because it is clean and it let us control as many parameters as possible in the material. The chemical formula for this strongly swelling smectite is $Na_{0.3}(Mg_{2.4}Li_{0.6})Si_4O_{10}F_2$.

The sample preparation of sodium fluorohectorite is divided in these three steps:

- Dissolving clay powder in distilled water
- Exchanging interlayer cations by adding NaCl and then removing the Cl^--ions
- Drying of clay samples under pressure

3.2.1 Dissolving in water

The fluorohectorite comes as a clay powder. The size of the grains is sub-mm and they consist of several clay platelets that are separated into individual clay particles when dissolved in water. We started mixing 120.2 g fluorohectorite with 500 ml distilled water with a pH=7.3, but we had to add more water to dissolve the powder. Finally we had a 1500 ml solution. The clay was stirred on a magnet stirrer for two days, and the pH-value in the solution was 11.7.

3.2.2 Exchanging interlayer cations

The amount of sodium ions that had to be added was calculated based on the amount of surface charge pr. unit cell, and the calculations are shown in Appendix B. We added 50.0 g NaCl, the salt was not dried before use. The solution was stirred over night. The next day the fluorohectorite was divided in two different phases, one clear water phase at the top and one white clay phase at the bottom, see figure 3.3.

Figure 3.3. Fluorohectorite is divided in two phases.

The temperature was increased to 60 ^oC, but then the clear phase at the top disappeared. The magnet stirrer was turned off, and the solution divided into two phases again. 25 ml of the clear phase was taken out, and the pH-value was measured to 11.3. The magnet stirrer was turned on and after another five days of stirring we turned the stirrer off. After the solution divided into two phases, the clear water phase was sucked out, as shown in picture 3.4. About 350 ml clear solution was removed.

Figure 3.4. Clear water phase is sucked out.

The clay phase was then dialysed in distilled water. Figure 3.5 shows the setup with the clay phase put inside the dialysis membrane. The membrane is closed in both ends with a locker and put in distilled water. A total of six such dialysis cylinders were made as seen in figure 3.6.

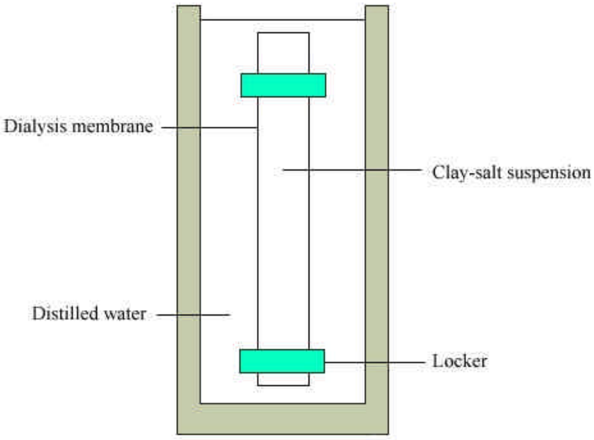

Figure 3.5. Dialysis cylinder set-up.

Figure 3.6. Dialysis cylinders.

The suspension was dialysed in distilled water for about one month. Every second day the distilled water was replaced, and the old dialysis water was tested for Cl$^-$-ions using the standard silver nitrate procedure. The pH-value in the old dialysis water was around 9-10. The pH was reduced below 7 by adding sulphuric acid to prevent formation of silver hydroxide (AgOH) when adding silver nitrate. A few drops of $AgNO_3$ were added and insoluble AgCl formed as a white powder. The formation of AgCl in this test decreased during the month of dialysis, but it did not disappear totally. This indicated that unwanted Cl$^-$-ions were removed from the clay-salt-suspension, although some of them were still present.

3.2.3 Drying of clay samples under pressure

Test samples of montmorillonite were used to examine the process of clay pressing. The procedure of filling up the cylinders is as the following. First the inner cylinder is turned upside-down. Then the metal plate with holes is put in. A paper filter is added, then the glass filter and on top another paper filter. The paper filter between the metal plate and the glass filter is there to make sure that the glass filter stays put. The next step is to thread the outer cylinder outside the inner. Then liquid clay is added, and a paper filter is put on top of it. Figure 3.7 shows a sketch of the clay-press at this point. The bottom ring of the outer cylinder has the glass filter attached using the paper filter so it will not drop when the ring is turned. When the bottom ring is screwed on the clay-press is turned. The first time we did this, the metal plate belonging to the inner cylinder fell down and clay was spoiled. The clay-press had to be modified using a thin metal rod inside the inner cylinder to prevent this from happening. This was only a few days before the trip to the USA, so we did not have time to make any samples before we left.

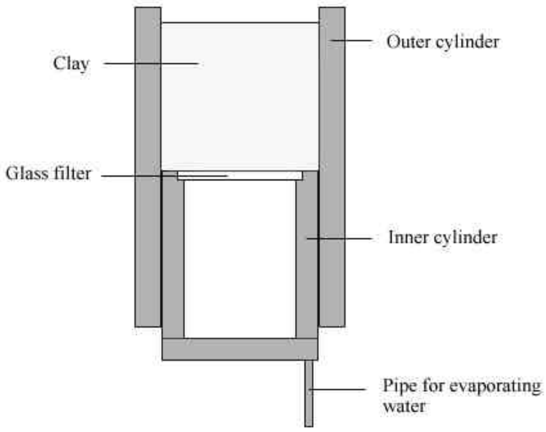

Figure 3.7. A see through view of the clay-press upside-down.

When we got back from the USA the experiments were done in collaboration with Magnus W. Haakestad because he is continuing my work with the clay pressing. After the modification of the clay-press, we used a hydraulic press we had lent from the physics workshop, shown in figure 3.8. The clay-press is placed inside a metal shield for safety.

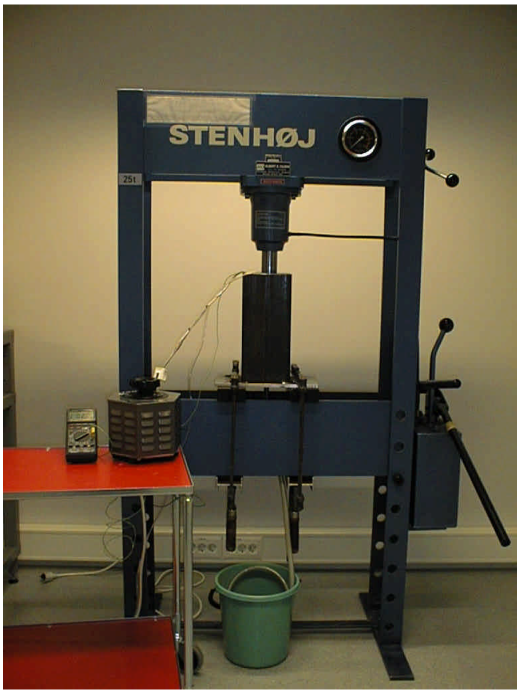

Figure 3.8. The hydraulic press.

When we had pressed for four days with temperature around 90 ^{o}C and a pressure up to 10 tons, the press was opened.

Figure 3.9. Leakage from the press.

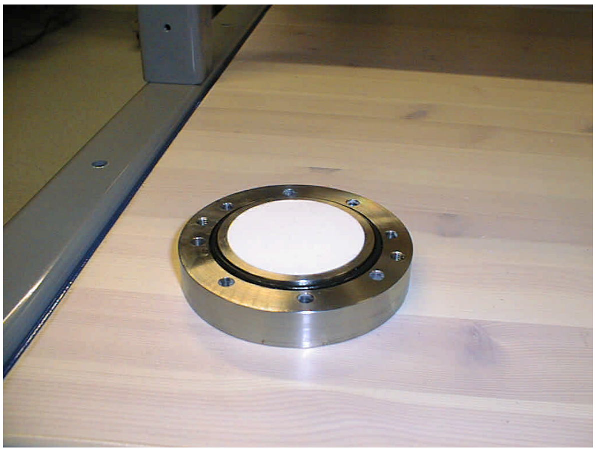

Figure 3.10. An o-ring is put in the bottom ring.

Nothing was left inside the press and all the clay had been pressed out through the opening between the bottom ring and the outer cylinder, see figure 3.9. The clay-press is again modified. This time an o-ring is put in the bottom ring as in figure 3.10. Yet another attempt of pressing is made. After seven days with temperature around 90 ^{o}C and pressure up to 10 tons, we opened the press. When we turned the press upside-down, a lot of water came out. This water had not vaporised. The piece of clay in the press was not dry. We put the press together again and heated up. It was probably better to keep the temperature above 100 ^{o}C to make sure that the water being pressed out would vaporise. The temperature was held between 110 and 120 degrees for another two days. It resulted in a hard piece of clay as shown in figure 3.11. It had a diameter of 68.8 mm, was 3.7 mm thick and weighed 25.0 g. The density was 1.8 g/cm^3.

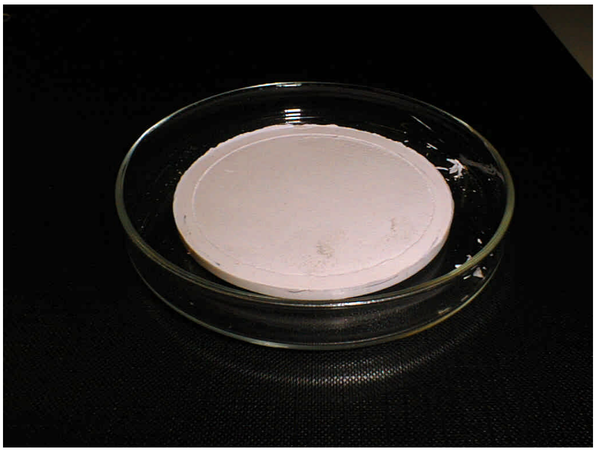

Figure 3.11. The first successfully pressed clay sample of montmorillonite.

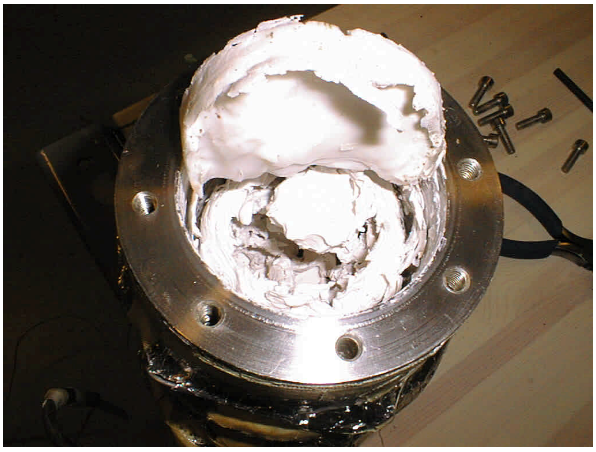

Figure 3.12. The inner cylinder is stuck and the clay has not been pressed together at all.

The inside of the outer cylinder and the outside of the inner cylinder had some scratches, and they seemed to have come before the press was pressed all the way in. A new attempt to press was made following the same procedure as the last time; heating up and maintaining the temperature around 110 degrees and keeping the pressure at 10 tons until it did not drop quicker than about half a ton after several hours, say 10 hours. This kind of pressure-drop is caused by the leakage due to the hydraulics, and the sample cannot be pressed further together. Again we used montmorillonite to make a test sample. This time the process went the same way, but we had a surprise when we opened the press. Figure 3.12 shows what we saw. The inner cylinder was stuck, and had not pressed the clay together at all, even though we had used a pressure of 10 tons. We tried to press out the inner cylinder, but even when we used up to 25 tons, it would not move. The press was destroyed, and we delivered it to the workshop because the inner cylinder had to be drilled out. Figure 3.13 shows the inside of the outer cylinder and the outside of the inner cylinder.

Figure 3.13. The inner cylinder is stuck.

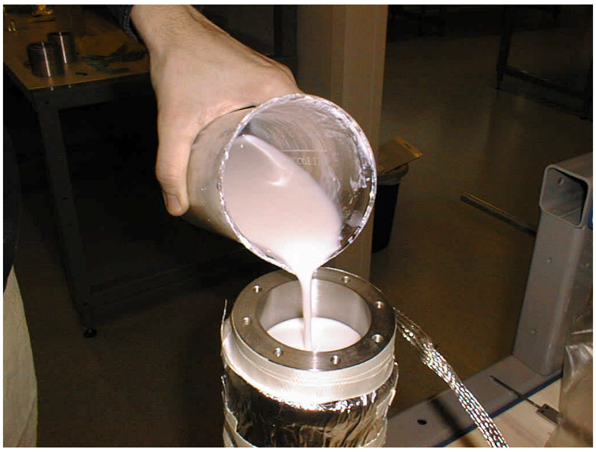

Figure 3.14. Montmorillonite is poured in.

The new inner cylinder was 3 cm shorter because mr. Bjølstad did not have a metal piece long enough to make an inner cylinder with the same dimensions as the previous one. Those extra 3 cm's were not necessary anyway. A new attempt to press 500 ml montmorillonite was made. Figure 3.14 shows when the montmorillonite is poured into the cylinder. The sample was pressed for four days with temperature round 105 degrees and at a pressure up to 10 tons. This sample weighed 82.0 g and had a density of 1.33 g/cm^3, and it is shown in figure 3.15. But the sample was not completely dry; we had taken it out to early. The clay press was sent down to the workshop again because the press had some small scratches we wanted to remove to prevent it from getting stuck again. Yet another attempt of pressing 500 ml montmorillonite were performed. This time the sample was pressed for six days with the same temperature end pressure as the last sample. The sample weighed 51.2 g and had a density of 1.72 g/cm^3, but it still was not completely dry.

Figure 3.15. Pressed montmorillonite, still wet.

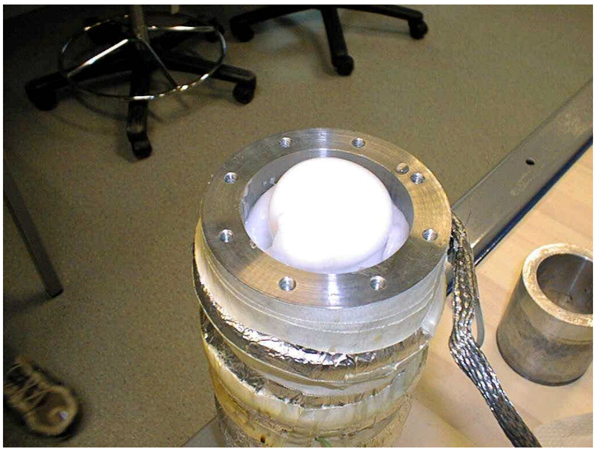

Figure 3.16. Sodium fluorohectorite is poured into the clay-press.

After this we started our first real attempt of pressing with sodium fluorohectorite. The consistence of the fluorohectorite was different and more like a gel compared to the montmorillonite, as shown in figure 3.16. The sample was pressed for as long as 14 days. The reason why we pressed for so long time was that the pressure kept dropping indicating that more water was pressed out. The cause of this was later found to be the hydraulic press itself, so our clay sample was finished several days before. The sample weighed 47.2 g and had a density of 1.75 g/cm^3. This was the first successful clay sample that was made of the sodium fluorohectorite. Figures 3.17 and 3.18 show the successfully prepared fluorohectorite.

Figure 3.17. First successfylly pressed sample of fluorohectorite. Picture taken by Magnus W. Haakestad.

Figure 3.18. Sodium fluorohectorite divided into pieces. Picture taken by Magnus W. Haakestad.

Further work with preparing clay samples is being performed by Magnus W. Haakestad and will be described in his diploma thesis.

3.3 Preparations before X-ray experiments

3.3.1 Beamline X22A

The beamlines are located in the National Synchrotron Light Source building at Brookhaven National Laboratory, Upton, New York. There are several different beamlines with different energy ranges used for different research techniques. Our beamline, the X22A, is in the category of surface scattering and X-ray reflectivity. It has an energy range of 10 keV and is used for in-plane diffraction and reflectivity studies of surfaces under electrochemical conditions and also of thin films and multilayers.

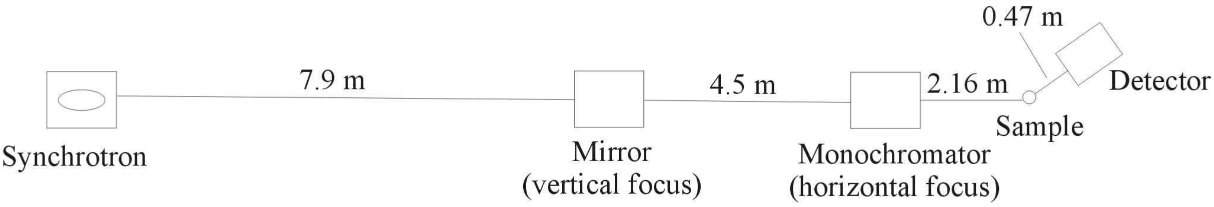

Figure 3.19. The optical configuration of beamline X22A.

Figure 3.19 shows the optical configuration for this beamline. Located 7.9 meters from the source is a platinum coated flat mirror focusing in the vertical. The monochromator is located 12.4 meter from the source. It is a Si(111) crystal monochromator focusing in the horizontal. The sample position is 14.56 m from the source. Between the monochromator and the sample the incident slits are located. Directly in front of the detector are the detector slits. The monitor gives a value for the incident radiation coming from the X-ray ring, while the detector counts the radiation scattered from the sample. Since the monitor value changes continuously due to the fact that the electrons disappear from the ring, the best way to measure the scattered intensity is always to divide detector by monitor. This is done for all scans and results presented in this report.

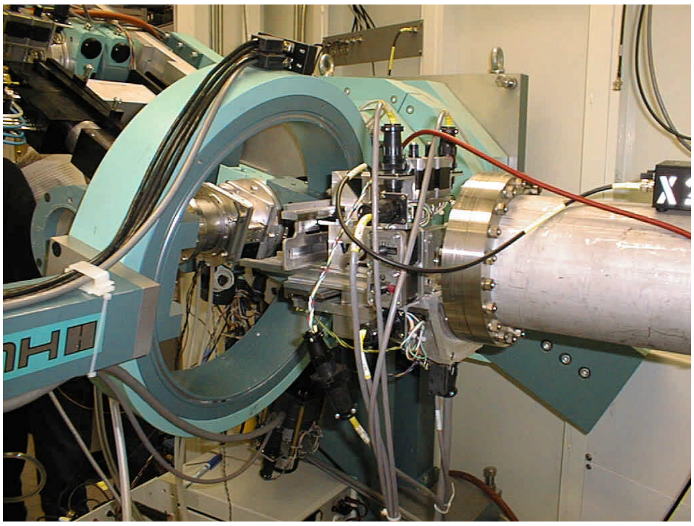

Figure 3.20. The diffractometer at beamline X22A.

Figure 3.20 shows the diffractometer that was used in the experiments. In the centre of the diffractometer the sample holder is located. The diffractometer operates as a four-circle diffractometer. This means that there are four angles that can be changed, and they are θ, 2θ, φ and χ. Figure 3.12 shows a sketch of a four-circle diffractometer.

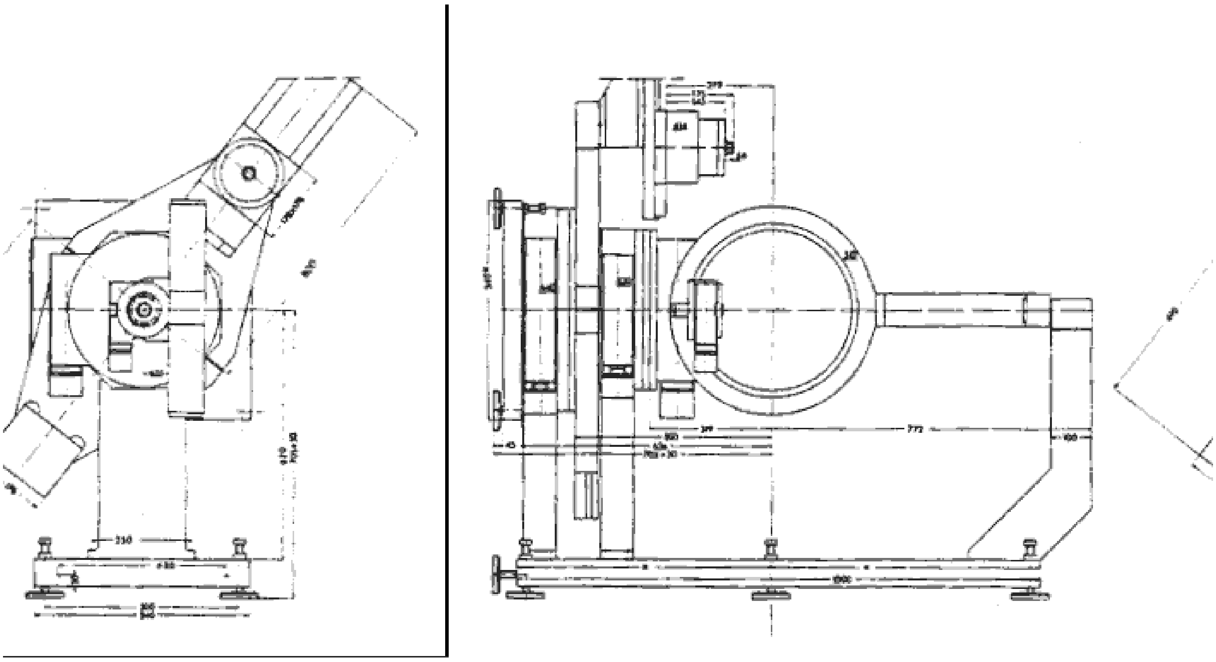

Figure 3.21. A sketch of a four-circle diffractometer. Figure taken from [17].

2θ is the angle through which the beam is scattered, and the other three angles are the ones orienting the sample. θ is the outermost circle with its axis of rotation coincident with that of 2θ. The χ circle is mounted on the θ circle, with its axis of rotation perpendicular to the θ axis. The φ circle is mounted on the χ circle such that its axis of rotation lies in the plane of the χ circle.

Most of the scans we took were so called q **- 2**q **scans**. When the sample is rotated an angle θ around the axis of the diffractometer, the detector has to rotate 2θ. Then we remain in Bragg position and measure the correct scattered intensity. This is because the sample acts much like a mirror when considering the reflection of the incident beam. Our scans are measured in the resiprocal space and are so called l-scans or q-scans.

Before the θ - 2θ scans rocking scans were performed to find the crystal distribution of the crystal fragments in the sample as a function of the angle. When a rocking scan is performed, only phi, or the detector, is moved and the intensity is plotted as a function of phi. Figure 3.22 shows how the crystal fragments might be aligned in a typical clay sample.

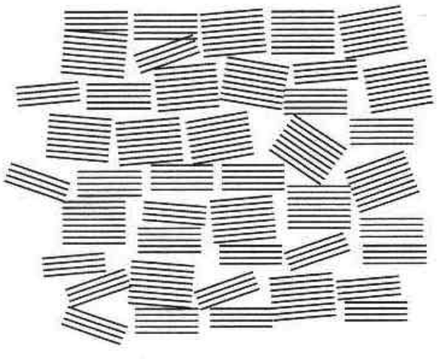

Figure 3.22. Crystal fragments in a clay film, taken from [16]

The best way to be positioned is to be at the top of the rocking curve, because here the scattered intensity is the largest. The particles in clay samples are randomly oriented, and this makes the rocking curve wide. The difference between micro pores and nano pores can also be explained looking at this figure. The nano pores are between the clay platelets in each of the crystallites, and the micro pores are larger spaces between these crystallites. In both these pore types water may intercalate and change the structure of the clay sample.

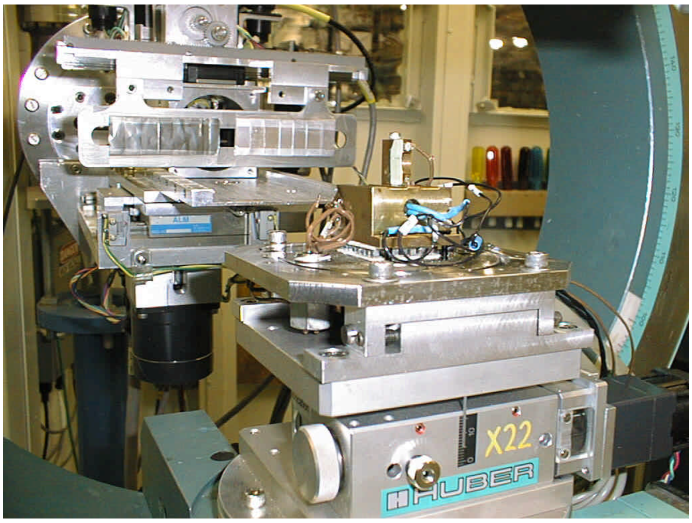

Figure 3.23. The diffractometer, looking at the bars.

The diffractometer is also equipped with bars and attenuators. A 16-bit attenuator is capable of reducing the incident radiation a factor of 4.65^{15}. In our experiment we used a higher attenuator value for the surface scattering sample than for the bulk sample, because more radiation was reflected than transmitted, and the detector can be destroyed if the intensity is too large. In addition to the attenuators, the bars, which consist of metal folium, reduce the radiation. Figure 3.23 shows these bars in the upper left of the picture. The bars are typically used when we want to move the detector passed the unscattered beam from the synchrotron ring.

3.3.2 Testing of the humidity measurer (RH sensor)

Figure 3.24 shows the humidity sensor when we tested it.

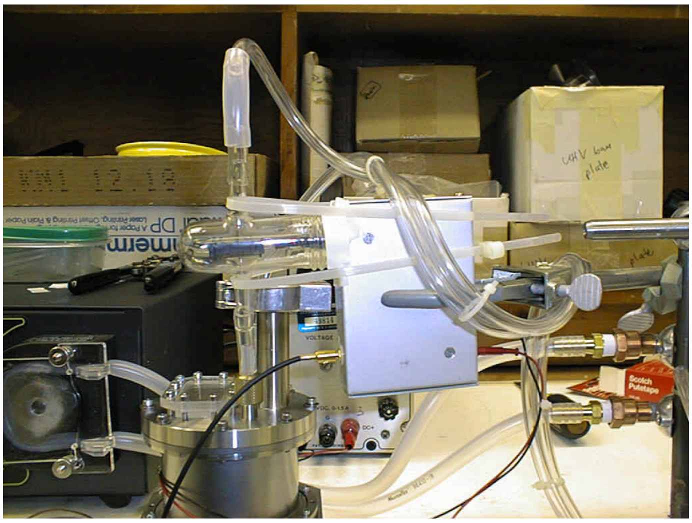

Figure 3.24. Testing of the RH sensor.

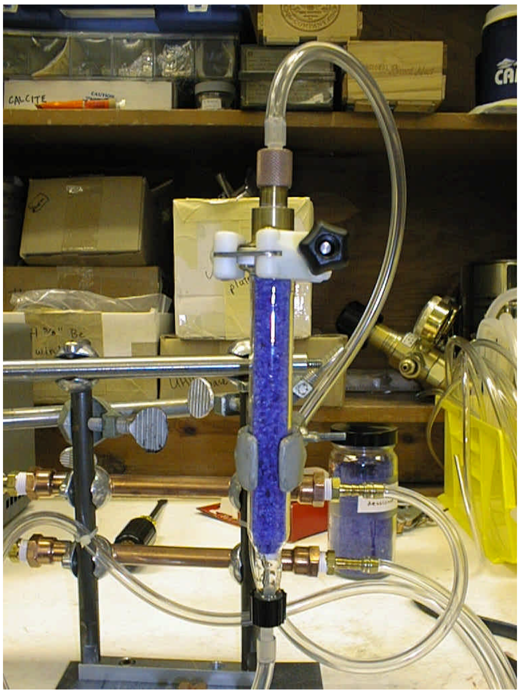

Figure 3.25. Silica gel dissicant.

Figure 3.26. Saturated salt solution.

To reduce the humidity the air passed through a silica gel dissicant as shown in figure 3.25. A gain in air-humidity was achieved when the air flow on top of a saturated solution of potassium sulphate, see figure 3.26. Making such a solution we need 12 g of K_2SO_4 pr. 100 ml water. When we tested the humidity sensor we found out that its readings were dependent of the air temperature. The best solution was to place the RH sensor in the air stream after the humidiator/silica gel and before the clay-chamber. More details about the RH sensor is found in appendix d.

Figure 3.27 shows the experimental set-up.

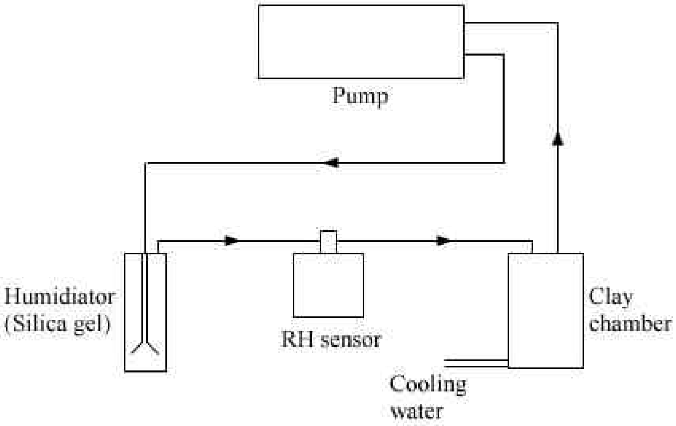

Figure 3.27. The best configuration for air flow through the system.

The readings from the RH sensor are in volts, around 0 V for 0% RH and 5 V for 100% RH.

3.3.3 Line-up

The first task was to centre the spectrometer in the beam and centre the incident slits around the beam. A special cone was placed at the centre of the spectrometer. Exposing X-ray paper at the peak of this cone for 20 seconds gave burn marks indicating where the beam hit. The spectrometer was rotated in all directions to make sure that the peak was centred. This was checked with burn paper and the telescope mounted on the table. The entire table with the spectrometer was adjusted to centre the beam on the centre of rotation of the spectrometer. The incident slits are located in front of the monochromator, and they are used to limit the width of the beam to make sure that the footprint on the sample is not larger than the sample itself. The X-ray beam might also be moving during the experiments, but if we only let the rays from the centre of the beam pass, this movement does not influence our results. The vertical incident gap was set to 0.34 mm and the horizontal incident gap to 0.5 mm.

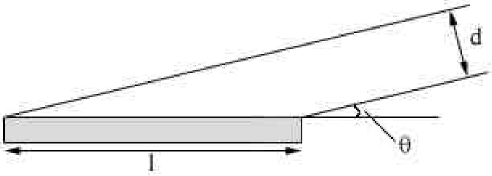

Figure 3.28. Definition of d, l and θ in equation (3.1) for the beam hitting the sample.

$$\sin\theta = \frac{d}{l} \Leftrightarrow l = \frac{0.34mm}{\sin 2^\circ} \approx 10mm \tag{3.1}$$

The smallest incoming angle the beam has at a peak is about 2 degrees, which gives a 10 mm footprint, according to figure 3.28 and equation (3.1) above. This meant that our sample could not be smaller than this to make sure that the entire beam would hit. The bulk sample is smaller than the sample used for surface scattering, about 4 mm wide. For small angles, smaller than about 5 degrees, the size of the bulk sample will limit the scattering volume.

The detector is capable of reading about 50000 counts/sec, but will not be destroyed before the counts exceed about 300000 counts/sec. The detector is fitted with both vertical and horizontal slits, without the slits the detector gap is 1 mm high and 4 mm wide. The slits prevent unwanted photons to enter the detector gap and falsify our readings. Different scans were taken with different values of dst and dsb (detector slit, top and bottom position).

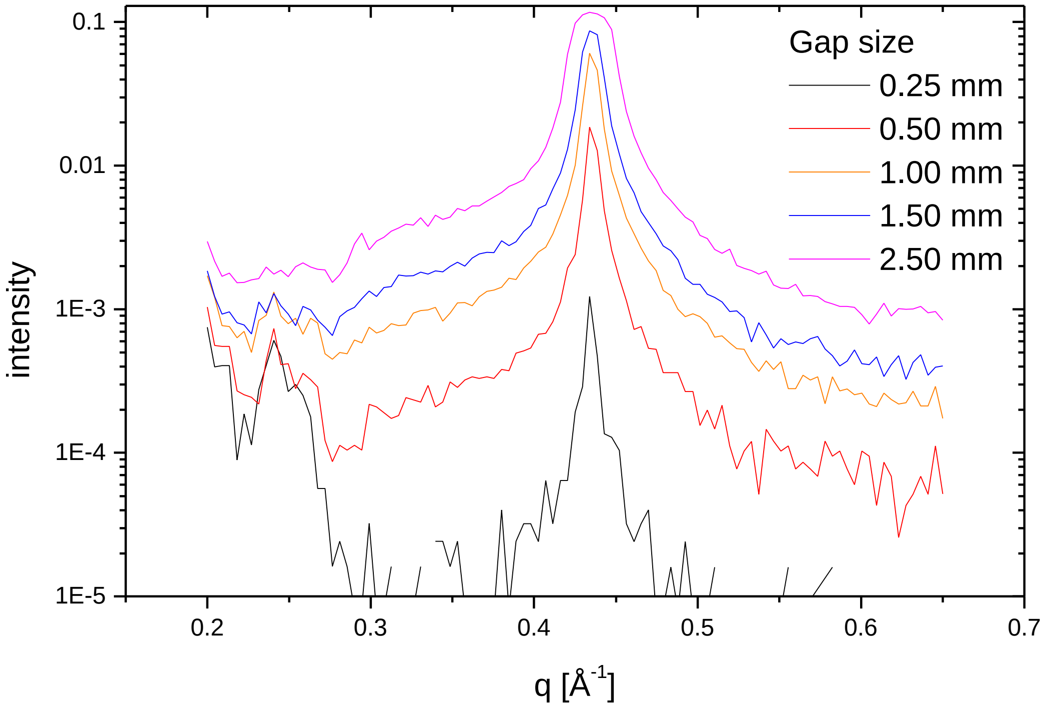

Figure 3.29. Scans with different gap sizes.

From figure 3.29 we see that a gap of 0.25, 0.5 and 1 mm only made a scale factor difference between the 001 scans taken, but when the gap was increased to 1.5 and 2.5 mm, the peaks became rounded having the same scaled tails as before. This meant that the opening was too large. A smaller opening gives a lower intensity of photons entering the detector pr. second, but this can be compensated by counting longer. The optimal gap was somewhere between 0.5 and 1 mm, but to make sure we would detect the peaks correctly, we chose the smallest of these two gaps. The values of dsr and dsl (detector slit, right and left position) were initially both 2, giving a gap of 4 mm. We tried to set them both to 0.5, but we did not see any change in ϕ or peak shapes, only the intensity changed. The resulting detector slit positions were as in table 3.1 below.

Direction	Slit Values	Gap size
Vertical	dst = 0.25	0.5 mm
	dsb = 0.25	
Horizontal	dsr = 2	4.0 mm
	dsl = 2	

Table 3.1. Final detector slit values

A rocking scan gives us the best angle for phi. When we are on the top of a rocking scan, we are in the position where the scattered intensity from the sample will be the largest because most clay platelets are favourably aligned to contribute to the scattered intensity.

3.4 X-ray diffraction experiments

Because we did not manage to make any samples of Na-fluorohectorite before we went to the USA, the X-ray experiments were done using Ni-fluorohectorite samples made by Simen Berg Lutnæs [16].

To be able to do measurements on a swelling clay sample, it is necessary to put the sample inside a chamber in which we can control the humidity and temperature. We used the chamber shown in figure 3.30. It is made of beryllium, a material that is transparent to X-rays. Inside the chamber the sample is glued to a block of copper with double stick tape. The copper block is in connection with a heating element and also a Peltier element for cooling to temperatures below room temperature.

Figure 3.30. Beryllium chamber.

The Peltier element's warm side is cooled with running cold water. Figure 3.31 shows what the chamber looks like with the top lid taken off. On the picture a flat sample for surface scattering is mounted on the copper block. Close to the sample the temperature is measured with a copper-constantan thermocouple mounted inside the block of copper. The temperature is measured using the Lake Shore 321 Autotuning Temperature Controller, see appendix e. It reads the temperature on the thermocouple and sends the value to the SPEC control software. The temperature controller also sets the temperature on the sample when it receives information from the SPEC program about the wanted temperature and sends the proper current through the heating element. The current through the Peltier element was set manually outside the hutch.

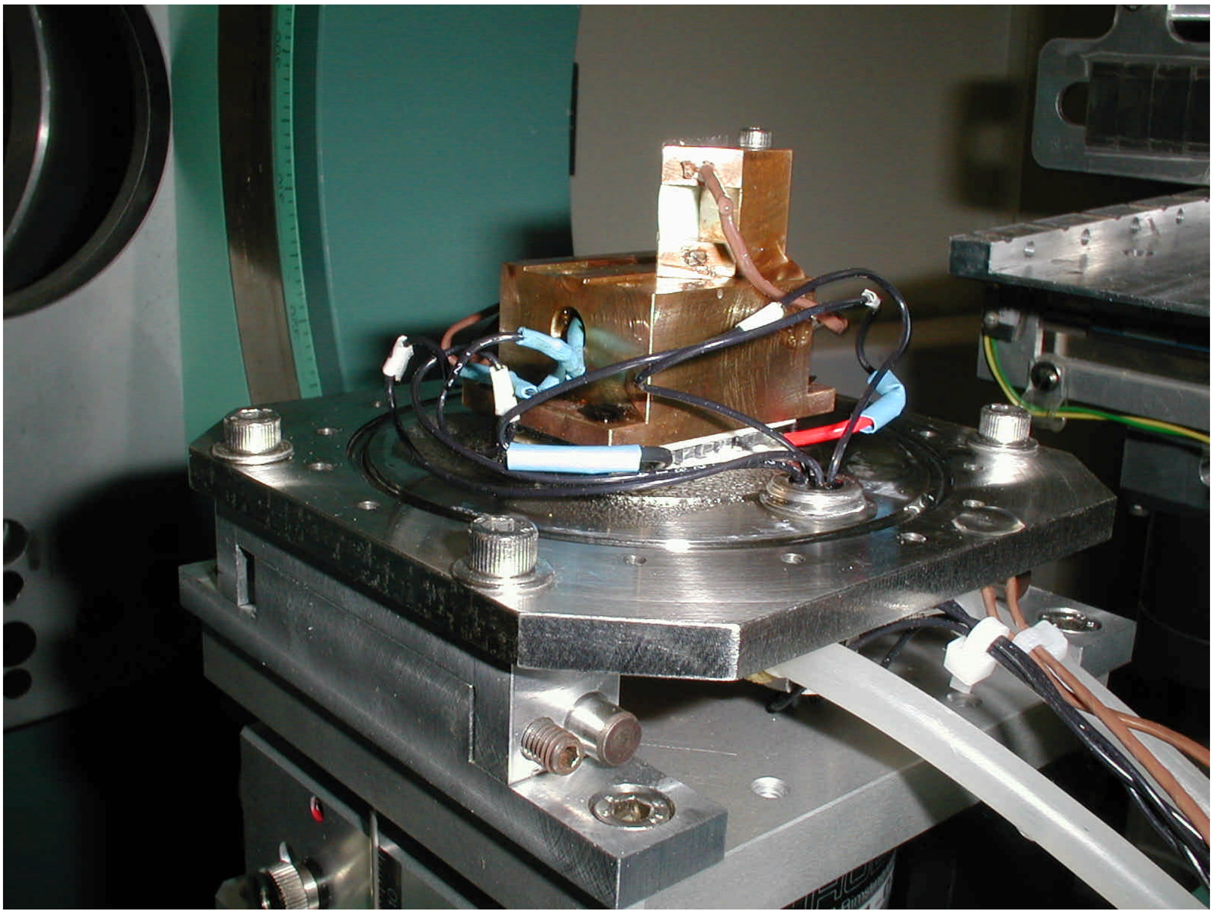

Figure 3.31. The copper block inside the beryllium chamber with a thin sample mounted on. This picture is taken by Kenneth Dahl Knudsen.

The humidity inside the chamber is controlled by pumping humid or dry air through the chamber. The Manostat Simon Varistaltic Pump, which is described in appendix c, pumps the air through either a saturated salt solution or a silica gel dissicant, as described in 3.3.2. A sensor for relative humidity, RH sensor, measures the RH in the air flowing into the chamber. Appendix d has more details about the RH sensor.

Figure 3.32 shows the sample for bulk scattering being mounted on the copper block, and on figure 3.33 the sample is covered with lead tape to prevent any contribution from surface scattering.

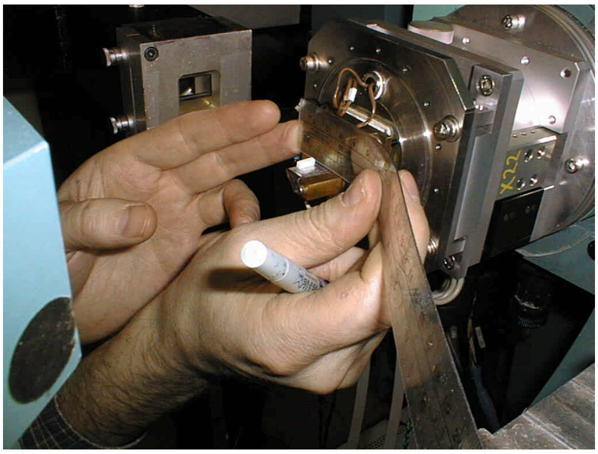

Figure 3.32. Bulk sample being mounted.

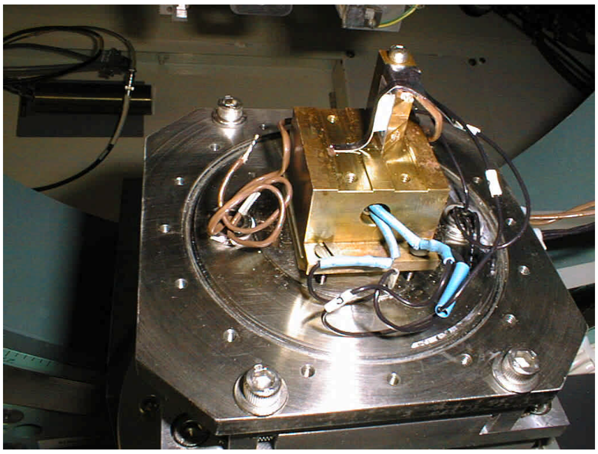

Figure 3.33. Lead tape is put on.

We started the experiments with the thin sample used for surface scattering. The sample position was adjusted to the top of the peak of the cone used to centre spectrometer. Scans were performed at different temperatures and humidity levels. The temperature was raised and lowered in small and large steps at both high and low relative humidity levels. After five days with experiments on the thin sample, we found that the sample had been destroyed and that it was bulky. This was caused by too much humidity when we had lowered the temperature down to 0^oC and stayed there with a high humidity level. The peak at the phi-scan (rocking scan) moved to 12^o indicating that the pieces in the clay were aligned in a different way. Since the sample became folded, we learned that these thin samples must not be glued to the copper at both ends. The first days we used this thin sample the chamber was not properly mounted. This resulted in a leakage from the chamber, which made it difficult to get the high and low humidity values we wanted. However with this extra ventilation of the chamber, we did not have any problems with excess water in the chamber and the clay was not being completely covered with water, thereby not destroyed.

After this we did similar experiments with the bulk sample for four days. Then we measured the background by placing the sample out of Bragg position for both low and high humidity levels. We also measured the background without the beryllium lid on. The last two days we did some more measurements with the thin sample.

4 RESULTS AND DISCUSSION

4.1 Resolution function

To measure the resolution function of the apparatus we have compared a scan of a quartz peak with a Bragg peak close to it. A quartz peak at position q=1.880 Å^{-1} was compared with a 004 peak at position q=1.822 Å^{-1} from the surface scattering sample. The q-values were adjusted so that the centre value of both peaks was q=0. The intensity of the quartz peak was modified to match the intensity of the 004 peak. Figure 4.1 below shows the result.

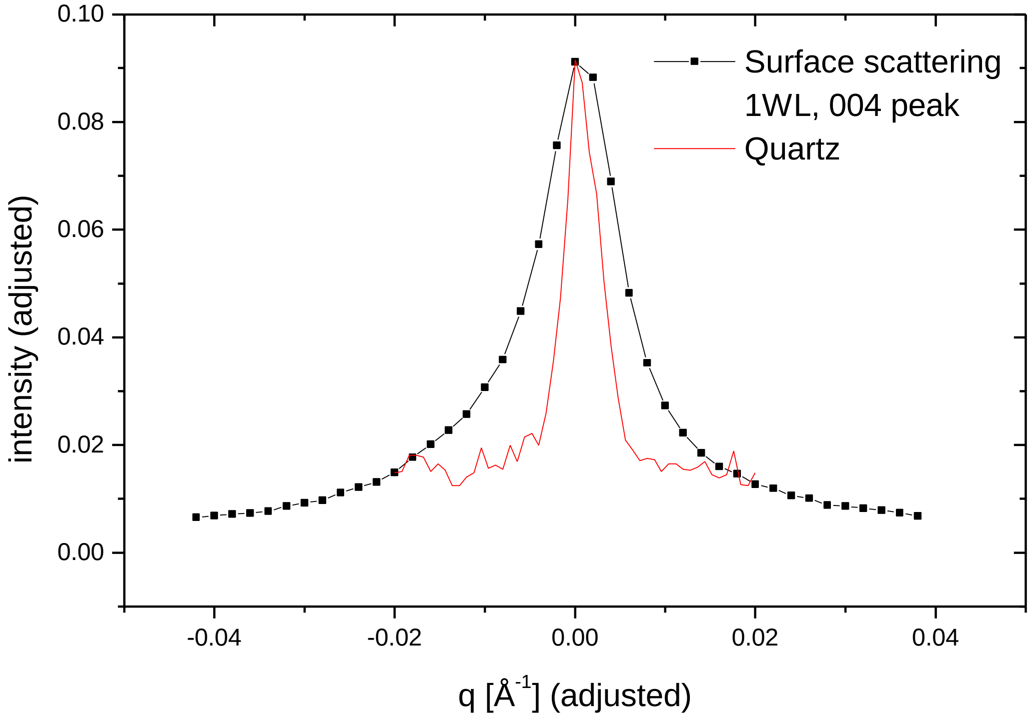

Figure 4.1. Resolution function of the apparatus.

The theoretical width of a delta function is given by the experimental resolution. Figure 4.2 shows how the beam scattered from the source is limited by the vertical slits before it enters the detector.

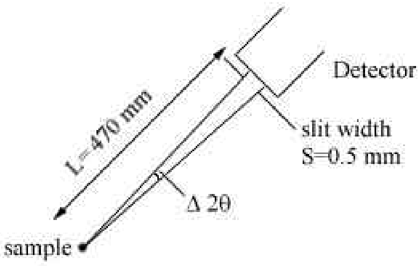

Figure 4.2. The beam scattered from the source.

The following approximation can be derived from the figure:

$$\Delta 2q \approx \frac{S}{L} \tag{4.1}$$

S is the vertical gap in front of the detector and L is the distance from the sample to the detector. The width, Δq, of a delta function can be estimated as:

$$\Delta q \approx \frac{4p}{l}\Delta q \approx \frac{2p}{l}\Delta 2q \approx \frac{2p}{l}\frac{S}{L} = \frac{6.283}{1.197}\cdot\frac{0.5}{470} = 0.0056Å^{-1} \tag{4.2}$$

When we fit a Gaussian to the quartz peak in figure 4.1, the width we get is 0.0040Å^{-1}, which is close to the theoretical value from equation (4.2). This means that our measured and calculated values of the experimental resolution correspond well. We would probably get a better result if the background of both graphs were subtracted before the peak intensities were matched. Due to lack of time this has not been done.

4.2 The impact of slit size on peak shapes

To test the importance of choosing slits that are narrow enough, we wanted to model how the measured peak shapes would look like with different slit sizes. First we tried to model a Gaussian moving over a Lorenz peak. The width of the Lorenz peak was set to 0.01 Å^{-1}, because that is the width of our typical 001 peaks. The resulting peak described as a function of q comes from the folding integral

$$\int_{-\infty}^{\infty} L(x)G(x+q)dx \tag{4.3}$$

where L and G are the Lorenz and Gauss functions. The answer to this integral is the Voigt-function, but Maple cannot handle the above integral. The slits were instead modelled as a square slit function because the Gaussian from the resolution function is close to such a function and this is easy to model.

$$\int_{q-\frac{w}{2}}^{q+\frac{w}{2}} L(x)dx \tag{4.4}$$

In our experiment the slits in front of the detector are the important factor for the solution function because the divergence coming in is much smaller than the broad rocking curve. In equation (4.4) the Lorenzian is integrated where the scattered intensity passes the square slit and the centre of the slit is at x=q. The parameter w is the slit width. In appendix h is the Maple-program that was used. Figure 4.3 shows the result for different slit sizes when the width of the Lorenz peak is 0.010 Å^{-1}.

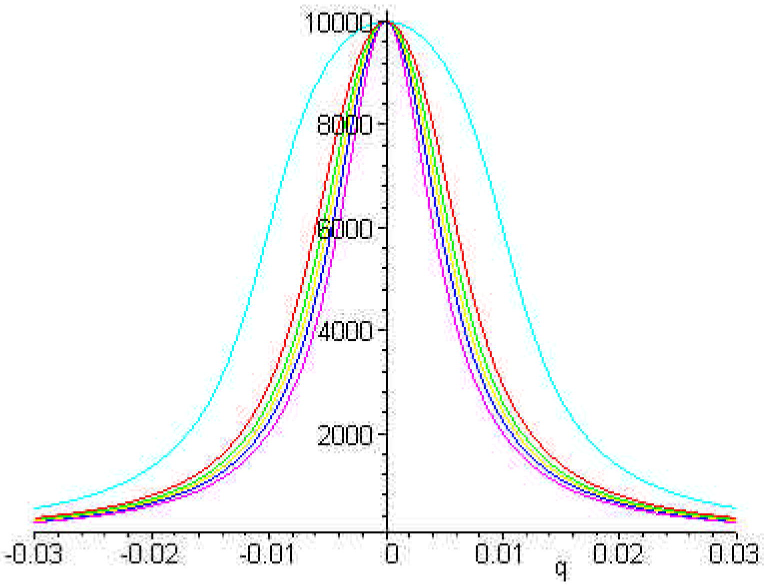

Figure 4.3. The impact of different slit sizes on measured peak widths for Lorenz peak with 0.010 Å^{-1} width.

In the figure the narrowest peak is the original distribution for a Lorenz peak with wl=0.010 Å^{-1} width, this is the pink line. The other five lines are the calculated widths using detector slits widths, ws, of wl/4, wl/3, 0.0040, wl/2 and finally wl/1 as the most broadened peak. The figure clearly shows that increasing slit widths give rounded peaks. The green line represents the broadening in our experiment. Compared with the pink line it is wider, and the measured intensity will at most be about 30% higher than the actual scattered intensity and the peak broadening is at most about 20%.

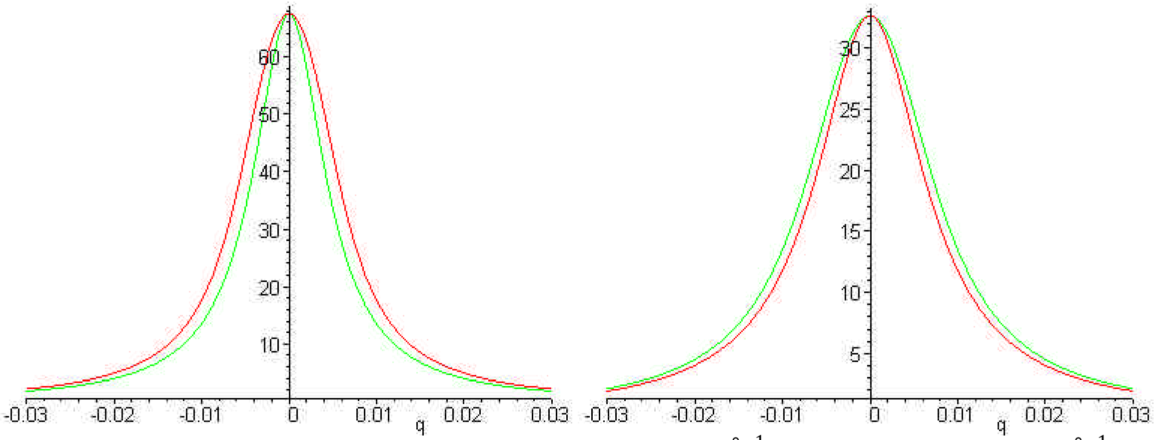

Figure 4.4. Broadening of peaks using slit width 0.0040 Å^{-1}. The left peak is 0.010 Å^{-1} wide and the right peak is 0.015 Å^{-1} wide. The inner line is in both cases the original scattered peak.

From figure 4.4 we see that the peak broadening with our slit width has larger effect on a narrow peak than on a wider peak. The narrowest peak has the width of a typical 001 peak while the widest could be a 005 peak.

4.3 Peak positions for the different water layers

Surface scattering

Figure 4.5 shows the results for the 001 peaks for 0, 1, 2 and 3 water layers for the surface scattering sample.

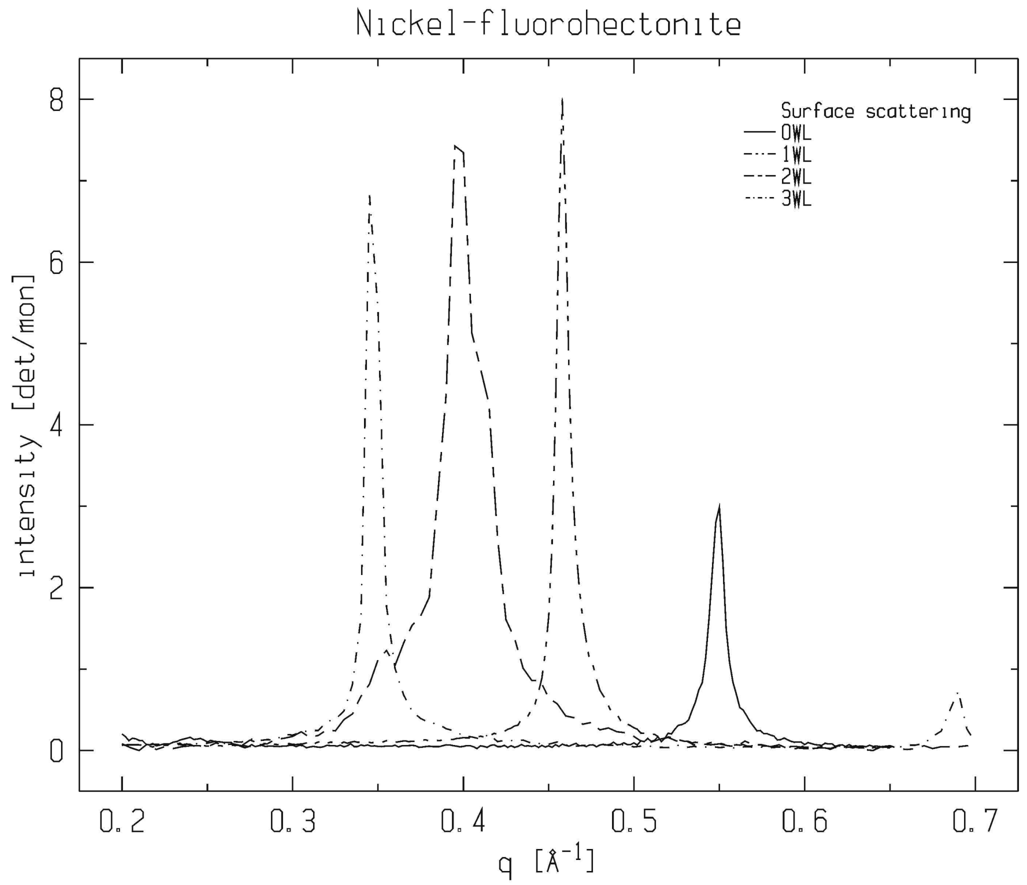

Figure 4.5. The different positions of the 001 peak for the surface scattering sample for different water layers.

The q-values of the different peaks are shown in table 4.1.

Water layers	Peak position [Å^{-1}]	d = 2π/q [Å]
0WL	q = 0.550	11.42
1WL	q = 0.458	13.72
2WL	q = 0.395	15.91
3WL	q = 0.345	18.21

Table 4.1. Peak positions for surface scattering

Also shown in the table is d, the separation between the layers. The distance is supposed to be proportional to the number of water layers. The difference between the d-values for each transition of water layer is found in table 4.2.

Water layer transition	Difference in d
0WL - 1WL	2.30
1WL - 2WL	2.19
2WL - 3WL	2.30

Table 4.2. Difference in d-value for transitions of water layers.

From these values we can see that the distance between the layers is proportional to the number of water layers. This also means that the peaks we have plotted are the correct representatives for each water layer.

Bulk scattering

For the bulk sample the situation is much the same.

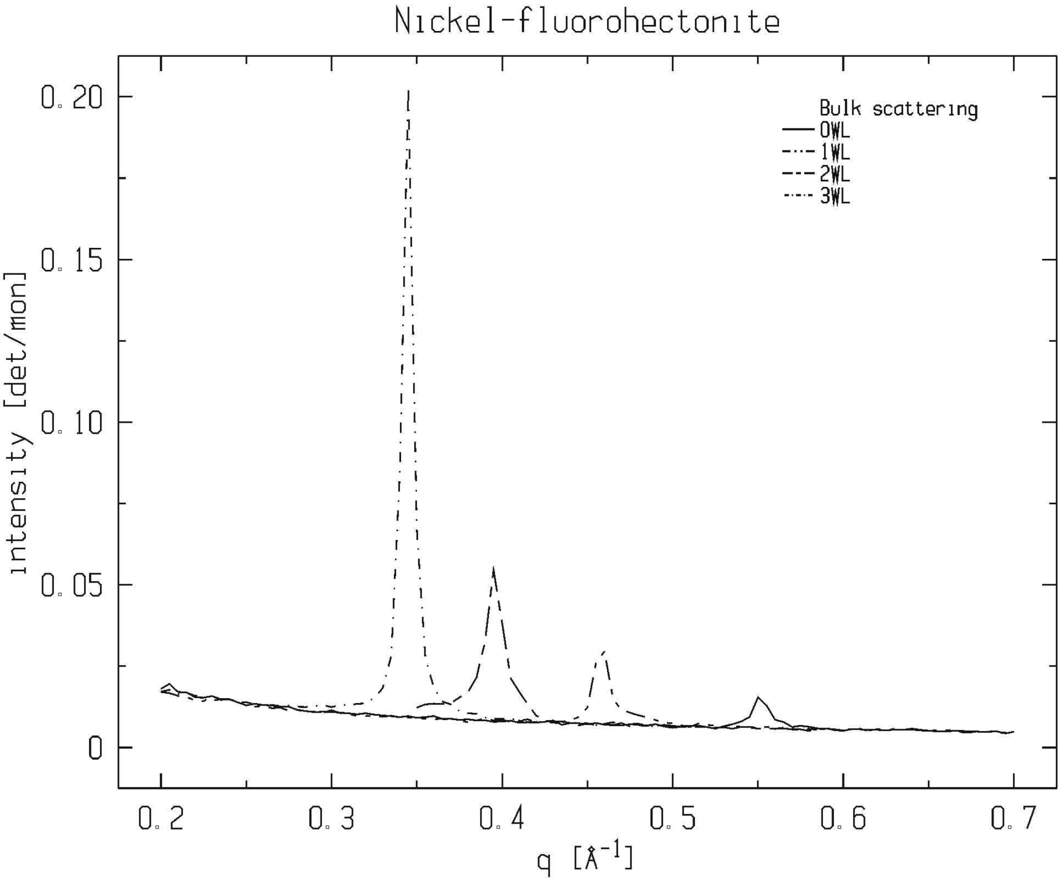

Figure 4.6. The different positions of the 001 peak for the bulk scattering sample for different water layers.

Figure 4.6 shows the results for the 001 peaks for 0, 1, 2 and 3 water layers. The background is not withdrawn. The q-values of the different peaks are shown in table 4.3.

Water layers	Peak position [Å^{-1}]	d = 2π/q [Å]
0WL	q = 0.550	11.42
1WL	q = 0.460	13.66
2WL	q = 0.395	15.91
3WL	q = 0.345	18.21

Table 4.3. Peak positions for bulk scattering

The difference between the d-values for each transition of water layer is found in table 4.4 below.

Water layer transition	Difference in d
0WL - 1WL	2.24
1WL - 2WL	2.25
2WL - 3WL	2.30

Table 4.4. Difference in d-value for transitions of water layers.

Even here the distances between the layers are proportional with the number of water layers.

From the two graphs we see that the peak for 2WL is broader for the surface sample than for the bulk sample. The peak is broader because 2WL is not a stabile situation for the thin sample. When we do not have a stabile situation, the Bragg peaks can be sum of peaks at different positions and not one peak at exactly one position as for a clean and stabile water layer situation. A sum of such peaks naturally gives a broader peak as result.

4.4 Williamson-Hall analysis

The Williamson-Hall analysis was performed for both the surface scattering and the bulk sample for the different water layers. The peaks were fitted to Lorenz and Gauss, but the values for Lorenz were the best. These values are presented in table 4.5 below.

Water layers	Peak	Surface scattering sample		Bulk sample	
		Centre	Width	Centre	Width
0WL	001	0.549	0.0111	0.552	0.0096
	002	1.098	0.0116	1.100	0.0049
	003	1.648	0.0125		
	004	2.196	0.0127	2.201	0.0191
	005	2.746	0.0154	2.749	0.0082
1WL	001	0.458	0.0091	0.459	0.0107
	002	0.912	0.0082		
	003	1.366	0.0115		
	004	1.822	0.0118	1.833	0.0118
	005	2.278	0.0131		
	006	2.737	0.0101	2.745	0.0192
2WL	001			0.396	0.0123
	002				
	003			1.187	0.0157
	004				
	005			1.981	0.0366
3WL	001	0.347	0.0079	0.344	0.0047
	002	0.688	0.0086	0.687	0.0068
	003	1.031	0.0102	1.029	0.0106
	004				
	005	1.716	0.0196	1.719	0.0100
	006	2.057	0.0279	2.058	0.0216
	007				
	008			2.764	0.0023

Table 4.5. Values for clean peaks fitted to Lorenz for the different water layers.

In this table the centre value is the centre position of the fitted Lorenzian and the width is the full width at half maximum (FWHM). Some of the cells are empty because satisfying data was lacking. It was not possible to find clean peaks for 2WL for the surface scattering sample because 2WL was not stable. From the table we see that the centre positions are very similar for the two sample types. The width of the peaks, however, is more different. But the same trend is present for both sample types; the width increases with increasing Bragg number.

If we call the centre value of the peaks x_c and the FWHM ω, the x- and y-values are given from the following equations according to the theory.

$$x = \frac{l}{4p} x_c \qquad y = \frac{l}{4p} w \tag{4.5}$$

For each sample and water layer the points (x,y) for each detectable Bragg peak are plotted with error bars.

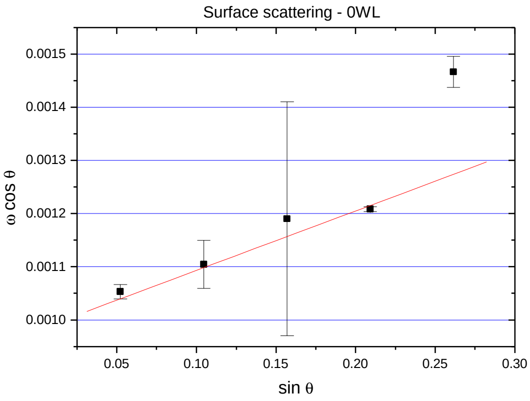

Figure 4.7. Surface scattering sample - 0WL.

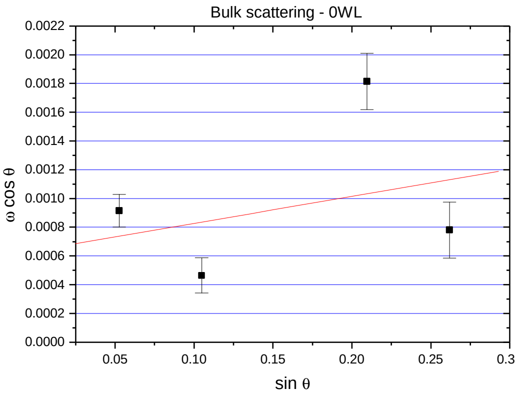

Figure 4.8. Bulk scattering sample - 0WL.

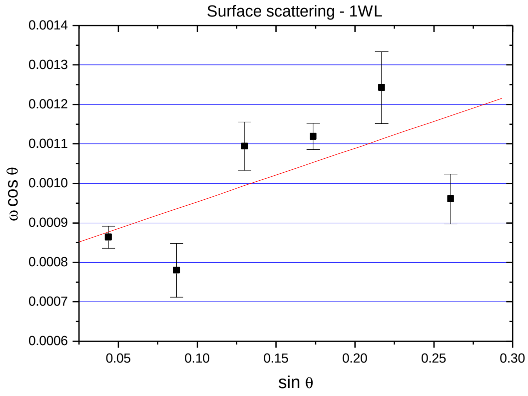

Figure 4.9. Surface scattering sample - 1WL.

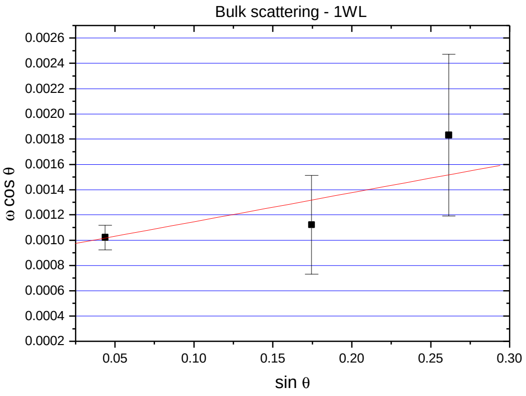

Figure 4.10. Bulk scattering sample - 1WL.

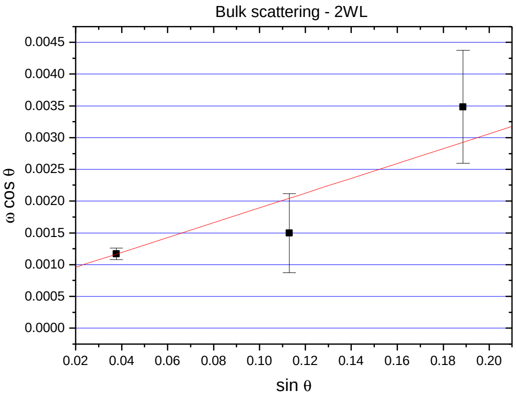

Figure 4.11. Bulk scattering sample - 2WL.

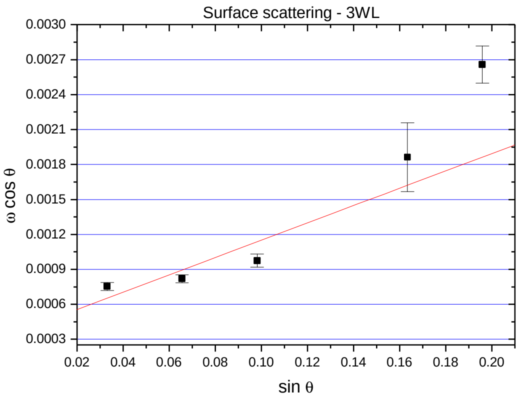

Figure 4.12 Surface scattering sample - 3WL.

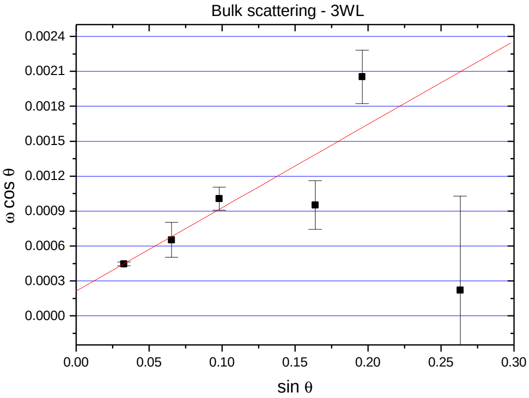

Figure 4.13. Bulk scattering sample - 3WL.

Table 4.6 shows the error in the peak width from the fitting to Lorenz.

Water layers	Peak	Sample type	
		Surface	Bulk
0WL	001	1.37379E-5	1.14260E-4
	002	4.52099E-5	1.21878E-4
	003	2.19951E-4	
	004	4.63792E-6	1.95195E-4
	005	2.93163E-5	1.95195E-4
1WL	001	4.23182E-5	9.71212E-5
	002	5.26844E-5	
	003	6.84485E-5	
	004	5.48439E-5	3.91341E-4
	005	8.18731E-5	
	006	4.04672E-5	6.40809E-4
2WL	001		8.89078E-5
	002		
	003		6.20814E-4
	004		
	005		8.89325E-4
3WL	001	3.52455E-5	1.57317E-5
	002	3.34059E-5	1.49490E-4
	003	5.64550E-5	9.90255E-5
	004		
	005	2.94220E-4	2.08525E-4
	006	1.59964E-4	2.28520E-4
	007		
	008		8.08391E-4

Table 4.6. Error in peak width from fitting to Lorenz. Used for error bars in plots and in the linear fits.

The y-intercepts, called A, from the linear fits for each of these plots, are shown in table 4.7 together with the d-value for the 001 peak and the resulting value for N. The q_{001} values are the ones from the fitted Lorenzian from table 4.5.

Water layer	Sample type	A	$d_{001} = 2\pi/q_{001}$	$N = \lambda/Ad$
0WL	Surface	9.810 E-4	11.444 Å	106.6
	Bulk	6.387 E-4	11.383 Å	164.6
1WL	Surface	8.175 E-4	13.709 Å	106.8
	Bulk	9.154 E-4	13.686 Å	95.5
2WL	Surface			
	Bulk	7.265 E-4	15.879 Å	103.7
3WL	Surface	4.046 E-4	18.090 Å	163.5
	Bulk	2.125 E-4	18.272 Å	308.2

Table 4.7. Values for N for the two samples at different layers of water.

When we look at the values for N we se that they are larger for 3WL. Even though that can be a coincidence, it is likely that the value is larger when there is more water in the samples. When more water is intercalated in the samples, the crystallites get larger, in fact up to twice their original size. There will eventually be a shortage of space in the sample, and some of the crystals stick together and make larger crystallites, increasing the value of N. If we look at the difference between the surface and the bulk sample, it is evident, at least for 0WL and 3WL, that the value of N is larger for the bulk sample. In the thin surface scattering sample the crystallites can move more freely, and the increasing crystallite size does not influence that much. Not so many crystals stick together, especially when water is added, and the value of N is lower.

Last minute discoveries have found that the error in the estimation of A varies from under 1/10 of the value of A and up to about 0.8. For instance the value N=164 for 0WL bulk cannot be trusted, because the error in A for this value is 5.28 E-4 compared to A=6.39 E-4. But for 0WL surface the error is 6.99 E-5, which makes ΔN about 8 and the estimated value of N should lie between 99 and 115. Another bad value is 3WL surface where the error in A is 1.95 E-4. Then we only values of N around 100 are to trust except for the 300-value for 3WL bulk which also must be taken into consideration as a probable correct value since the error here is 6.44 E-5.

4.5 The determination of n

Our subject was to decide the value of n in equation (1.6) for our clay samples. For a single crystal n=0, and for random powders n=1. For our samples the value of n was assumed to be somewhere in between 0 and 1.

4.5.1 G factor

The way to approach this problem was first to find the G^2 factor. From equation (1.5) we see that we had to find the atomic structure factors, the positions and the number of the different elements in nickelfluorohectorite to do that.

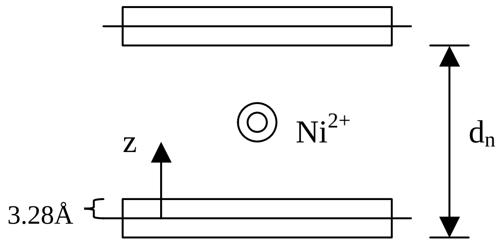

Figure 4.14. Position of Ni^{2+} between the sheets.

In figure 4.14 d_n denotes the distance between the layers, ranging from 11.4 to 18.2 Å, for the different number of water layers n. The clay sheets are 6.56 Å thick [15]. The positions of the elements are measured relative to the centre of the layer, and because of symmetry only half of each unit cell's positions are used. For all water layers it is assumed that the Ni^{2+}-ions are positioned in the centre between the sheets, and their positions are $d_n/2$. Monte Carlo simulations for Mg-smectites [12] have shown that the Mg^{2+}-ion stays in the centre position between the layers, and we assume that this also is the case for the Ni^{2+}-ion, because it has about the same ionic radius. This is not the case for the water molecules. In an article about the hydration of montmorillonite [13] a density distribution of water molecules as a distance z from the sheet is given. We do not know exactly how the distribution in our clay sample is, so we could have used this modelled distribution. But instead we made a simpler model placing the water molecules symmetrically between the layers as shown in figure 4.15.

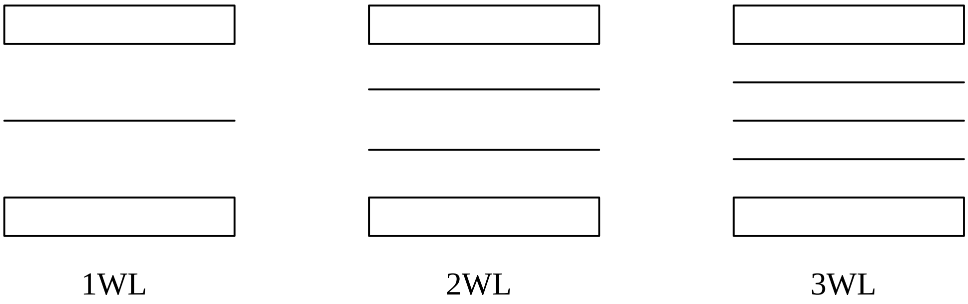

Figure 4.15. The dashed lines represent the positions of water molecules for the different water layers. The distance between the clay sheets is of course increasing with the number of water layers.

Table 4.8 has the z-values for the positions of water and Ni for the different water layers.

Water layers	d_n	z_{water} [Å]	z_{Ni}
0WL	11.4 Å	-	5.70 Å
1WL	13.7 Å	6.85	6.85 Å
2WL	15.9 Å	6.39 / (9.50)	7.95 Å
3WL	18.2 Å	6.19 / 9.10 / (12.01)	9.10 Å

Table 4.8. The positions of water and Ni for the different water layers.

For the positions of water for 2 and 3WL we do not use the values in parenthesis because of symmetry.

In appendix f is the Maple-file used to calculate G^2 for the different water layers.

4.5.2 Lorenz-polarisation factor

The factor was written in terms of q as this equation:

$$L_f = \frac{1-2Q^2+2Q^4}{(1-Q^2)Q^{n+1}}, \quad Q = \frac{l}{4p}\cdot q \tag{4.6}$$

4.5.3 Fitting with Origin

From the clean scans for the different layers of water the background was withdrawn. The scans were also adjusted for the attenuator used in the experiment. The background was estimated from the background scans that were taken when the sample was not in Bragg position. Because of a drop in the background radiation around q=0.9, we estimated a different background for q-values higher and lower than this value. For the upper half there are two estimated backgrounds, one for RH low and one for RH high. For the lower half there is only one estimated background because it was similar for high and low RH.

$$y = y_0 + A\cdot e^{-\frac{q}{t}} \tag{4.7}$$

This equation is used to model the background and the values of the parameters are shown in table 4.9 below.

q-value	RH	y_0	A	t
q < 0.9	low & high	0.00314	0.0193	0.2464
q > 0.9	low	0	0.0071	0.8019
"	high	0	0.0067	0.8217

Table 4.9. Baseline parameters.

In appendix g are the functions we tried to fit in Origin. The first attempt to fit these equations failed because we tried to fit them using the all the data points instead of only the peak values, and the results were not stable. The peak values from the bulk and the surface scattering sample were used at the same time for the different water layers. To be able to do this, the peak values for the thin sample were adjusted so that the 001 peaks for both sample types got the same peak value.

The figures 4.16 to 4.19 show the result from the fitting with Origin. For all water layers except 2WL peak values for both the surface scattering and the bulk scattering sample are used. But 2WL for the surface scattering was not stable and these peaks are not included. For

0, 1 and 3WL nLI is held at 0.3 because when the parameter was let loose it either went up to over 0.5 or even below 0, which is an unrealistic value. The values for v1, v2 and v3 are the ones used in the Maple-file in appendix f. For 0WL the value of n is stopped at the boundary set at n=1, but for the other water layers we see that the fitted value of n is around 0.85. For 1WL the drawn line is wrong because of some bug in Origin, but the fitting is ok.

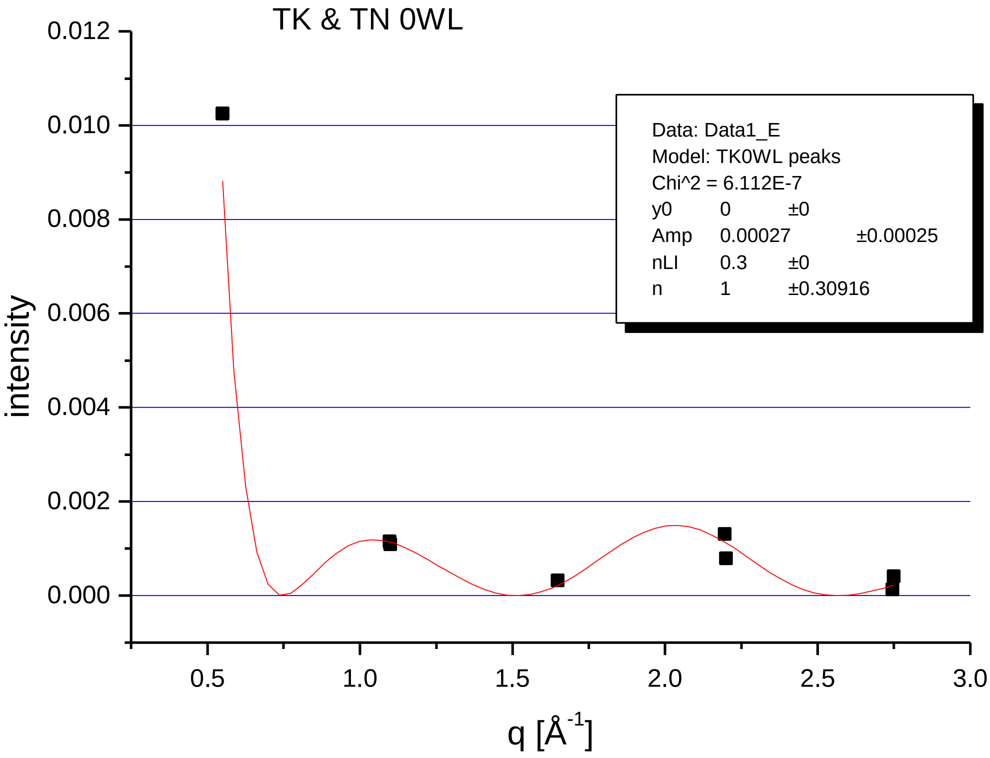

Figure 4.16. Fitting in Origin for 0WL. nLI is held at 0.3 and n ≤ 1.

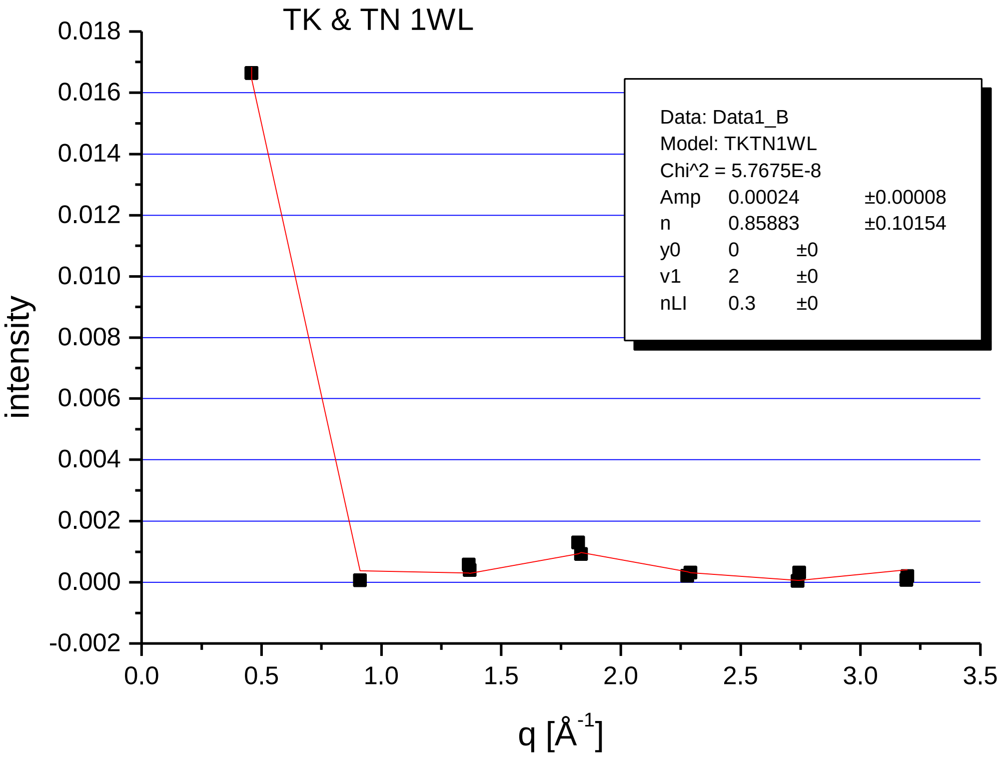

Figure 4.17. Fitting in Origin for 1WL. nLI=0.3 and n is a free parameter.

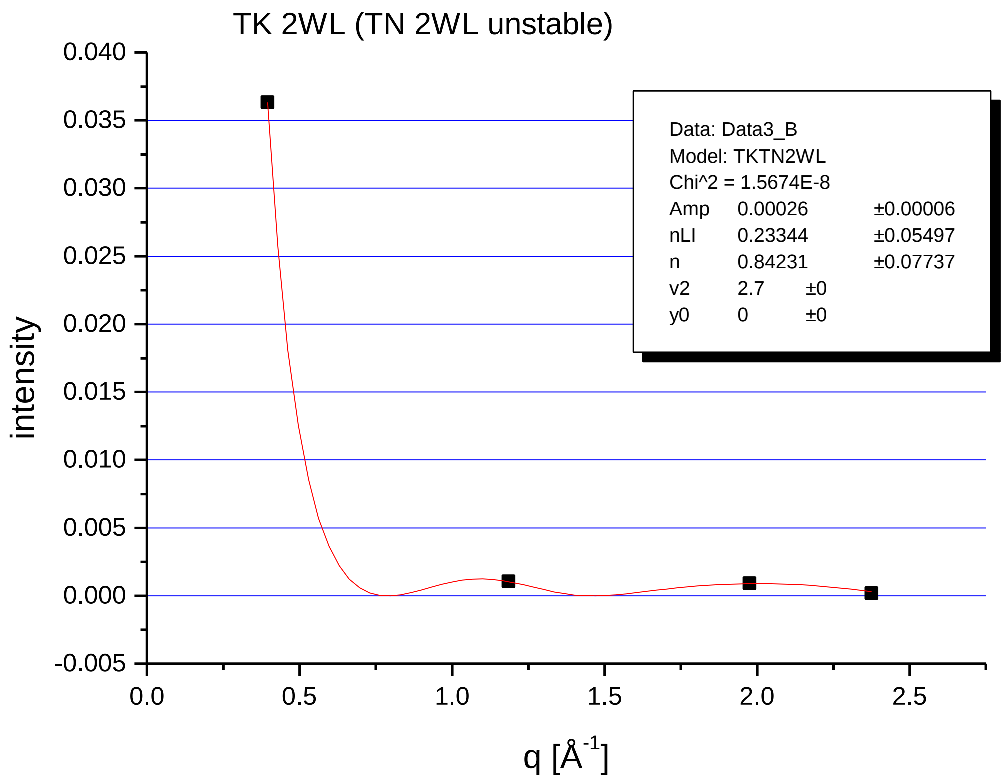

Figure 4.18. Fitting in Origin for 2WL. Only the peak values from the bulk sample are used. Both nLI and n are free parameters.

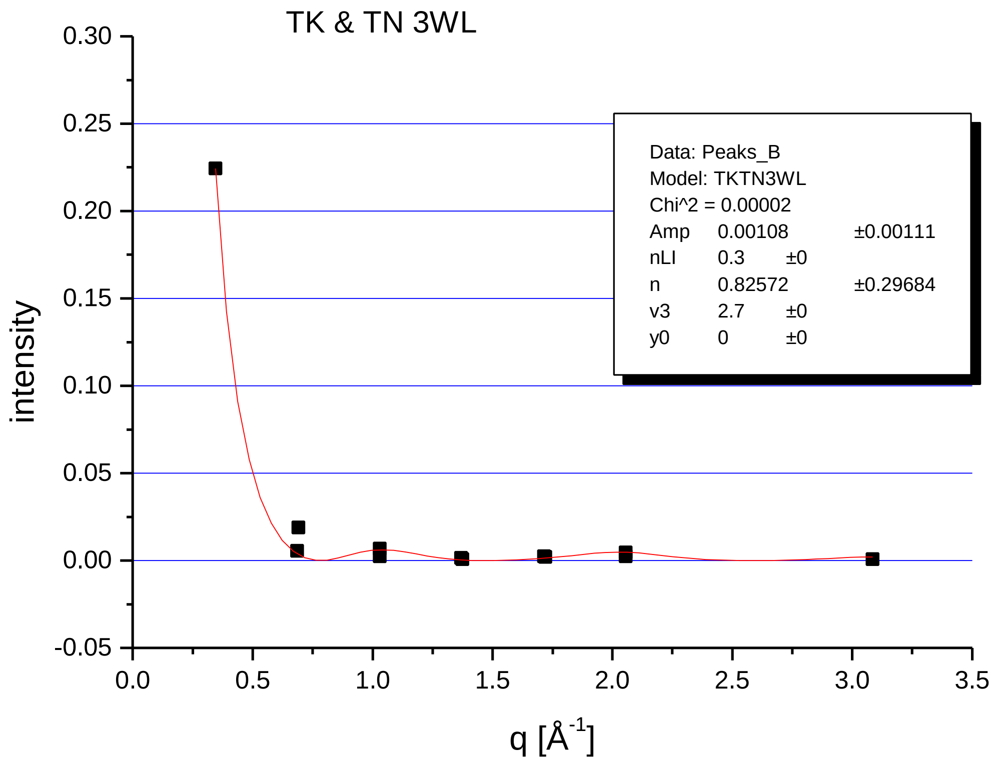

Figure 4.19. Fitting in Origin for 3WL. nLI=0.3.

When it comes to deciding the value of n it is best to do this for 0WL because we do not have the uncertainty about how much water we must include. For 0WL the graph shows a value of n=1. Another way of deciding the value is to start and hold n at different values from 0.5 to 1.0 and then estimate the other parameters before n is let loose. This is a good idea because it is not always favourable to let all the parameters free at once. Table 4.10 below shows the Chi-squared value for fitting 0WL when n is held at different values.

n	Chi^2
0.5	6.659 E-8
0.6	5.028 E-8
0.7	3.947 E-8
0.8	3.277 E-8
0.9	2.907 E-8
1.0	2.756 E-8

Table 4.10. Chi^2 values for 0WL when fitting with Origin and n is held at different values.

From this table we see that the smallest Chi^2 value is for n=1.0. When n was let loose, the value ended at 1.04 for all the different start values of n. For the nickelfluorohectorite sample n=1 is the most likely value for n indicating that the particles in our sample are randomly organised.

The value of n can also be different for the different water layers according to [15]. We see from the figures that the value for n for 1, 2 and 3 water layers is close to 0.85, but the uncertainty in this value is larger than the value for 0WL because we do not know the exact amount of water intercalated in these samples.

5 CONCLUSION

5.1 Conclusions from the experiments

The X-ray diffraction experiments on Ni-fluorohectonite have given us information about the intercalation of water in this synthetic smectite clay. A much deeper analysis of the material from these experiments would have given us more information. Nevertheless the analysis that has been done has given us some valuable information about this specific clay sample.

In the analysis of the peak position it is clear that the d-spacing between the clay sheets is linearly dependent on the number of water layers that are intercalated. When an additional layer of water is intercalated, the distance between the clay platelets increase with about 2.3 Å, equivalent to the size of a water molecule. This happens for all the three water layer transitions and for both the surface scattering sample and the bulk sample. The peak positions for the different water layers are also equal for the two sample types. From the 2WL peaks, especially for the surface scattering sample, we can see that the 2WL situation is not stabile because the peak is broader. This was also evident when searching for 2WL, because the water layer transition sometimes went so fast that we were not able to catch it on an X-ray scan before it disappeared. The analysis does not show the connection between the position of the different Bragg peaks for a given water layer. But from the work with the data files it is clear that the connection is in accordance with the theory. It says that the positions for a 00n peak is at a q-value n times the value for the 001 peak. From table 4.5 from the Williamson-Hall analysis we can see that the centres of the fitted Lorenz functions obey this rule, even though this is not properly analysed.

The impact of slit size on peak shapes have been studied more carefully. The peak broadening from our choice of slit width does that our measured peaks have a higher intensity and are broader than the ideally measured peaks. The effect on the peak widths is about 20%. In out data analysis we should have taken into consideration that we in reality have a convolution between a Gaussian and a Lorenzian, which would have accounted for the broader peaks and given us better results.

From the Williamson-Hall analysis it is difficult to say something exact about the value of N, the number of sheets in each particle, but the value is around 100 for 0, 1 and 2WL. If we can trust the data for 3WL the value of N must be dependent on the amount of water intercalated in the samples and therefore larger. This is reasonable because more water gives larger crystals that might stick together and create larger crystals. It is harder to find any relation between sample type and the value of N, but it is logical to think that for the bulk sample it is easier for the particles to grow into a neighbouring particle than for the surface sample.

Our clay particles are most likely fairly randomly organised according to the analysis of n, the parameter deciding if our sample acts like a single crystal or a random powder. For 0WL the value is 1 and for the other water layers it is close to 0.85. A reduction in the value of n with increasing amount of water in the sample can be explained by the fact that crystals that have grown larger have less freedom to move and their orientation will be dependent on the orientation of crystals nearby.

5.2 Further work suggested

The next natural step in the analysis of the X-ray data would be to investigate the dynamics of water transport. The studies presented in this thesis cover the intercalation of water but do not look into the field of dynamics. It is interesting to know how fast the water layer transitions occur and to find out about the difference in transition speeds between the thin and the thick sample. Also important is to find out at which temperatures the different water layers are stabile for the two sample types and whether or not the temperature is on its way up or down.

From the work with the data files and also when looking at the graphs when the X-ray experiments were performed, we can find situations where 1.5 WL and 2.5 WL occur. These kinds of transition situations have not been investigated any more than that we have seen them and know they are present in our data. An example is shown in figure 5.1.

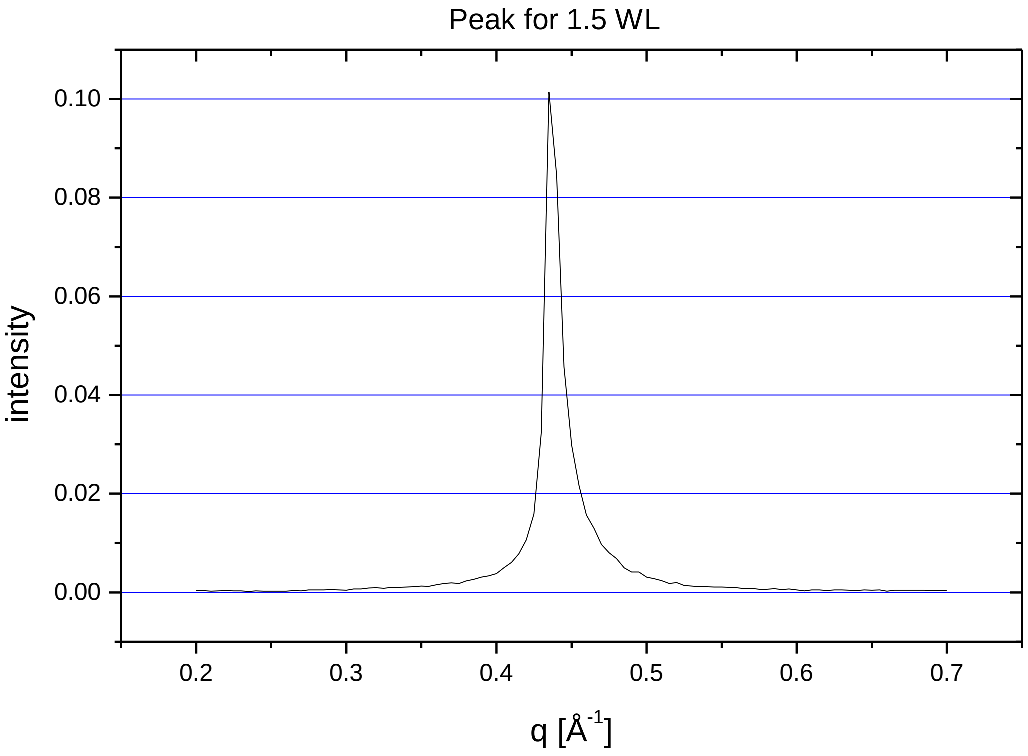

Figure 5.1. An example of a 1.5 WL peak with centre position q=0.435 Å^{-1}.

Some small amount of time was used to check if so called Hendricks-Teller situations occurred in our collected data. But if they do, the effects are hardly measurable, and they are small compared to the data from the Na-fluorohectonite samples.

An interesting discovery that we made is the ripples around the 006 peak, as in figure 5.2. These ripples should be analysed to find out what they really are.

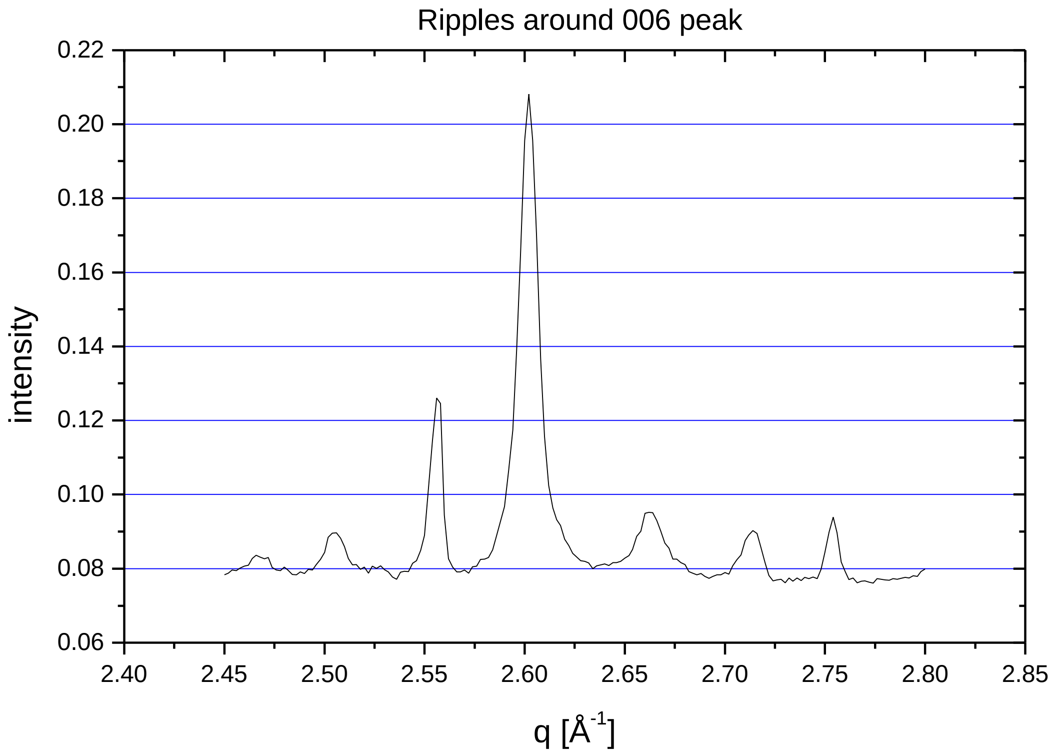

Figure 5.2. Ripples around 006 peak.

APPENDIX

Appendix A

The figures A.1 and A.2 show the design of the clay-press.

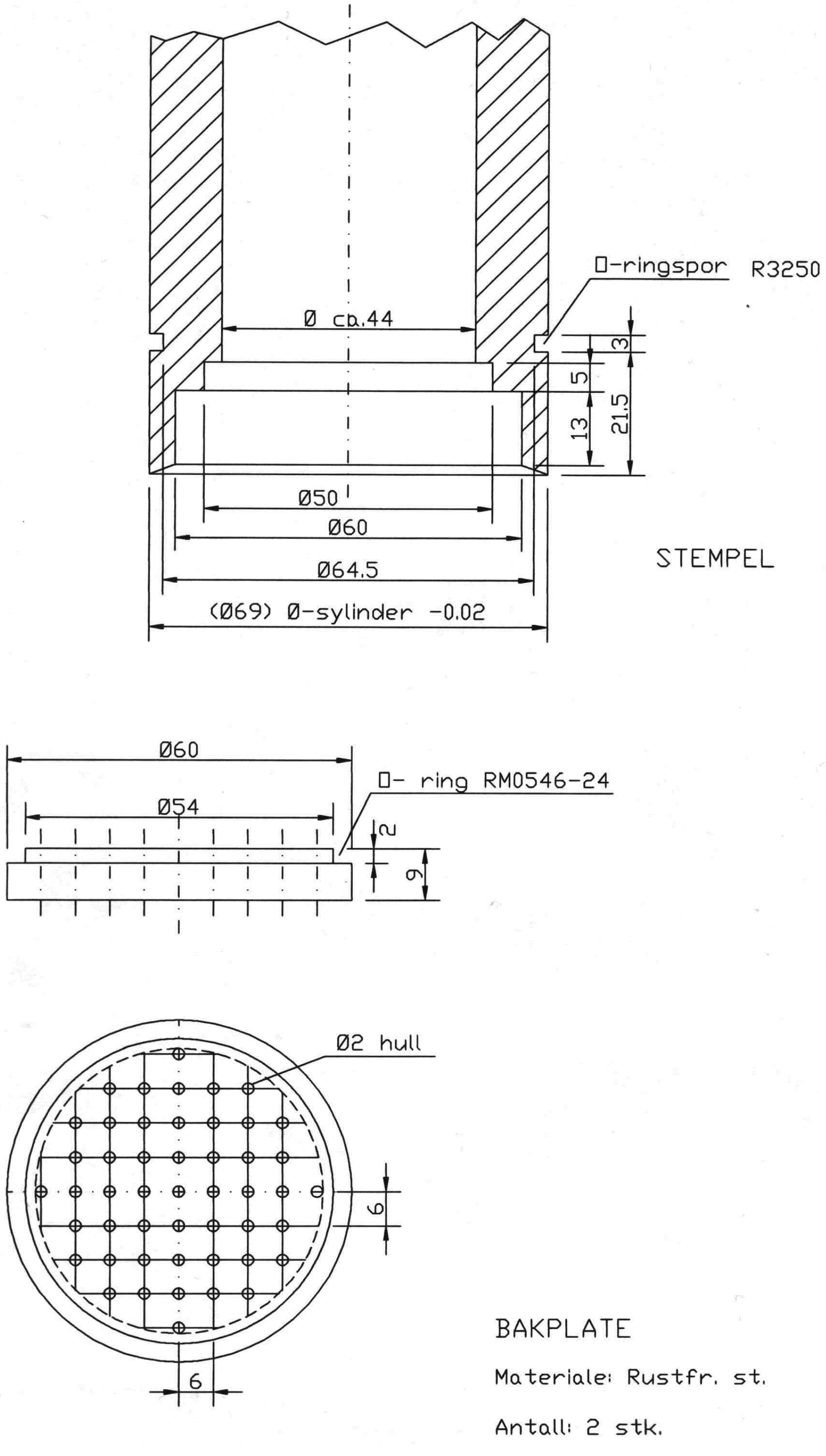

Figure A.1. Design of the inner cylinder and the metal plate with holes in it.

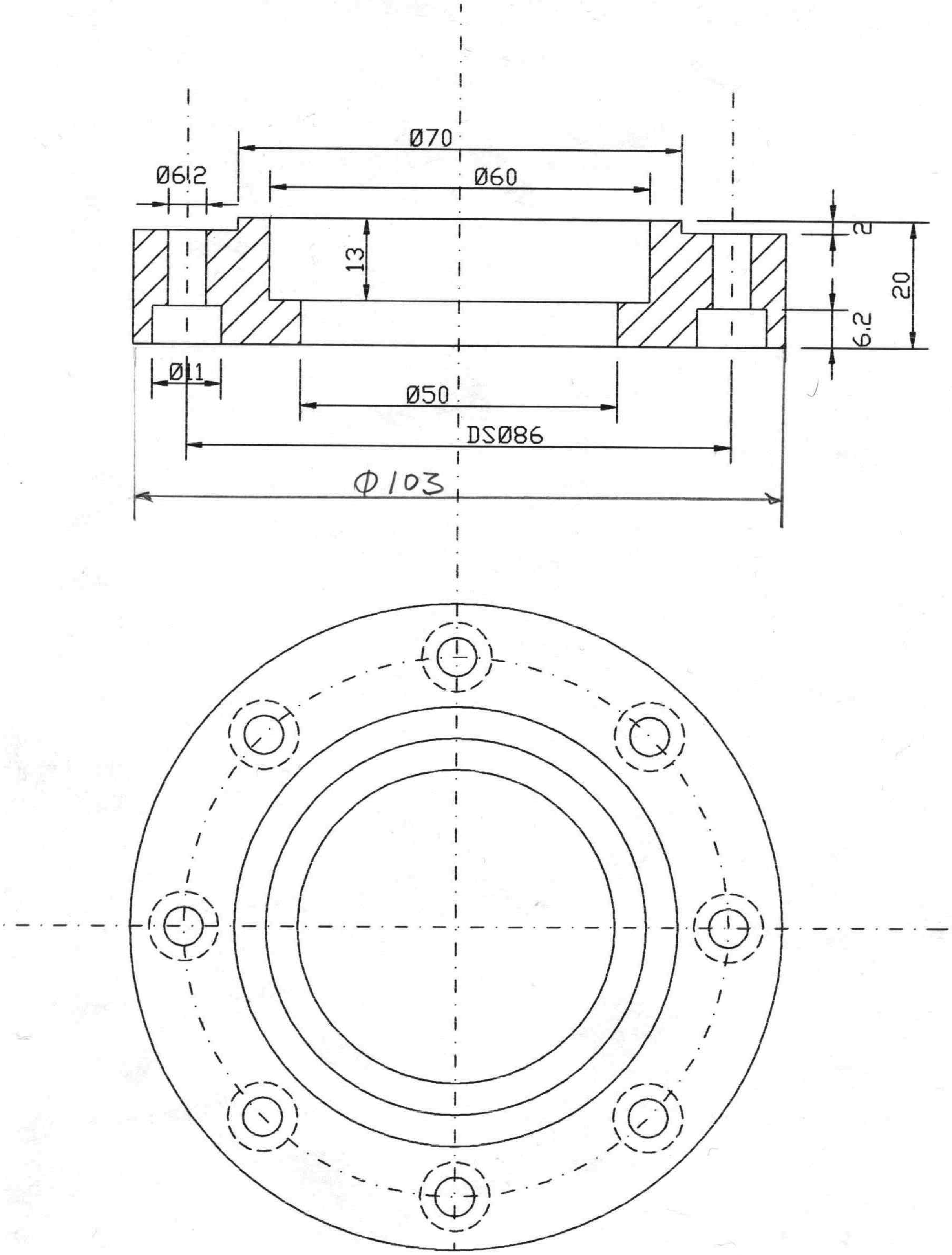

Figure A.2. The design of the bottom ring belonging to the outer cylinder.

Appendix B

Calculation of the amount NaCl to be added

To make sure that all the unwanted cations are replaced we add ten times as many cations as the amount needed to balance the negative surface charge. This must be done to make sure that the cations in the clay suspension are dominated by the cations coming from the added salt. The following assumptions are made:

- Density of clay sheet, $\rho \approx 2.8$ g/cm^3
- Surface charge, $\sigma \approx 1.2e$ pr. unit cell
- Volume of one unit cell, $V_u \approx (10 Å)^3$

The amount fluorohectorite used was m=120.2 g. The number of unit cells can now be calculated:

$$N = \frac{m}{rV_u} = 4.2929E22 \tag{B.1}$$

The charge of each unit cell is given by σ and the total charge equals to:

$$q = Ns = 5.1515E22e \tag{B.2}$$

The number of ions with charge 1e needed to balance this charge is:

$$\begin{aligned} N_A &= 6.022E23 mol^{-1} \\ n &= \frac{q}{N_A} = 0.08554 mol \end{aligned} \tag{B.3}$$

We need 10n mol sodium ions or

$$m_{NaCl} = 0.8554 mol \cdot 58.5 \frac{g}{mol} = \underline{50.0 g} \tag{B.4}$$

50.0 g NaCl.

Appendix C

Manostat Simon Varistaltic Pump

We used the Manostat Simon Varistaltic Pump to circulate air through the beryllium chamber. Figure C.1 shows the pump when we were testing the humidiator/dessicant before we started the experiments. The pump has regulation of flow speed and flow direction. The rotation creates a pressure that can pump either a gas or a fluid.

Figure C.1. Simon Varistaltic Pump.

With the analog speed potentiometer one can adjust the rotation speed from 24 to 720 rpm giving a flow from 5 to 3000 ml/min. The dimensions of the pump are about 25 x 25 x 15 cm and it weighs 6.8 kg.

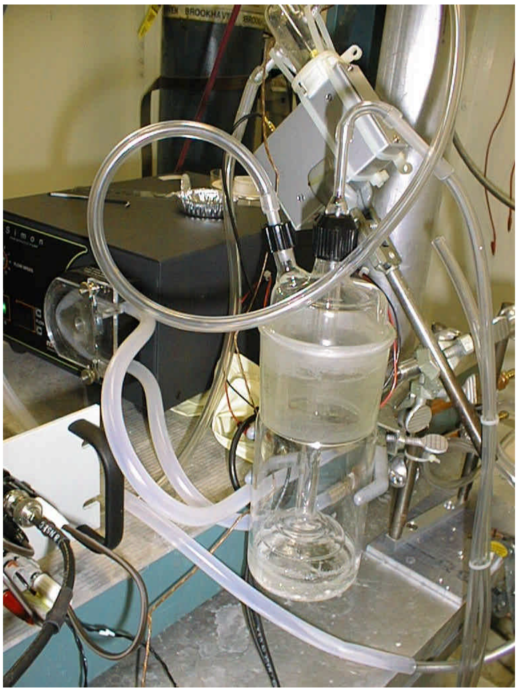

Figure C.2. The pump in place.

Figure C.2 to the left, shows the pump with connections inside the hutch. The silicone tube going through the pump was replaced several times during the experiments because the tube started to leak.

Appendix D

RH sensor

The RH sensor is a G-CAP Capacitive Relative Humidity Sensor from General Eastern. According to the commercial it gives a "low cost and high performance humidity sensing with superior long-term reliability". The features say that the temperature coefficient is less than 0.05% RH/^{o}C which would insure "accurate and reliable operation in applications where the final product will be exposed to wide temperature ranges". The operating temperature is -40^o to 100^{o}C. Our experience with the sensor, however, was different.

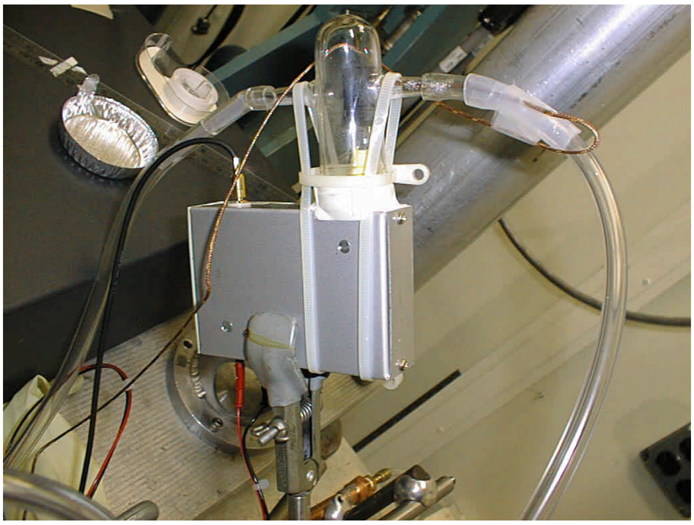

Figure D.1. RH sensor inside the hutch.

Figure D.1 shows the RH sensor mounted to the electronic circuit that converts the capacitive output from the sensor to a voltage between 0 and 5 V. The RH sensor is the black piece of plastic inside the glass tube at the top centre of the figure. With this placement the sensor is in the middle of the air stream going into the chamber. The dimensions of the sensor are 2.5 x 1.3 x 0.5 cm.

When the sensor was placed in the air stream going into the chamber and we used the saturated salt solution, a typical reading from the electronics would be 4.7 V. This indicated a high RH, which was correct. But when we turned the direction of the air stream, the readings dropped to around 2.5 V. It was not logical, because the humidity in the air should be exactly the same. The only thing that was different was the air temperature. Since we were heating the copper block to around 100 degrees, the air coming out of the chamber was 10 degrees warmer than the air going in. We took the sensor out of the glass tube and blew hot air from a hair-dryer on it, and as suspected, the readings dropped quickly. Some of the change in the measured RH can be explained by the fact that the RH sensor was not calibrated for the higher temperature, but this cannot be the whole cause to the change.

Appendix E

Lake Shore 321 Autotuning Temperature Controller

Figure E.1 shows the front panel of the temperature controller. It has a serial interface and can communicate with the SPEC program. For instance the temperature is set to 40^{o}C on the temperature controller when one types the command `te 40` in the SPEC program.

Figure E.1. Lake Shore Autotuning Temperature Controller.

The voltage out from the temperature controller is decided from the current and the wanted temperature together with three parameters set on the temperature controller. These parameters are the ones in the PID-function used to control the voltage output.

More information about the temperature controller can be found on Lake Shore's web-page http://www.lakeshore.com.

Appendix F

Maple-file for the calculation of G^2. The file is followed with an explanation.

Nickelfluorohectorite.mws

```
> restart;
```

The parameters v1, v2 and v3 are fitting parameters representing the amount of water for 1, 2 and 3 WL

```
> v1:=2; v2:=2.7; v3:=2.7;
```

$$v1 := 2$$

$$v2 := 2.7$$

$$v3 := 2.7$$

Debye-Waller factors:

```
> W:=1.58;
dw:=exp(-W*(q/(4.0*evalf(Pi)))^2);
```

$$\mathrm{W} := 1.58$$

$$dw := \mathbf{e}^{(-.01000546688\,q^2)}$$

Atomic structure factors:

```
> f[H]:=1;      f[Li]:=3.00;  f[O]:=8.05;   f[F]:=9.07;
f[Ni]:=27.54; f[Mg]:=12.17; f[Si]:=14.29;
```

$$f_H := 1$$

$$f_{Li} := 3.00$$

$$f_{\mathrm{O}} := 8.05$$

$$f_F := 9.07$$

$$f_{Ni} := 27.54$$

$$f_{Mg} := 12.17$$

$$f_{\mathrm{Si}} := 14.29$$

Notation: *Number* of such element **= n[** *element* **[** *layer, time of coming up* **]]**

The number of atoms in the clay platelet

```
> nLi:=0.3;
> n[Si[0,1]]:=2;       n[F[0,1]]:=1;  n[Li[0,1]]:=nLi;
n[Mg[0,1]]:=1.5-nLi; n[O[0,1]]:=2;  n[O[0,2]]:=3;
```

$$nLi := .3$$

$$n_{\mathrm{Si}_{0,\,1}} := 2$$

$$n_{F_{0,\,1}} := 1$$

$$n_{Li_{0,\,1}} := .3$$

$$n_{Mg_{0,\,1}} := 1.2$$

$$n_{O_{0,1}} := 2$$

$$n_{O_{0,2}} := 3$$

The number of nickel ions for 0, 1, 2 and 3 WL. The nickel ion is always in the middle between the layers.

```
> nNi:=nLi/2;
n[Ni[0,1]]:=nNi;
n[Ni[1,1]]:=nNi;
n[Ni[2,1]]:=nNi;
n[Ni[3,1]]:=nNi;
```

$$nNi := .1500000000$$

$$n_{Ni_{0,1}} := .1500000000$$

$$n_{Ni_{1,1}} := .1500000000$$

$$n_{Ni_{2,1}} := .1500000000$$

$$n_{Ni_{3,1}} := .1500000000$$

The number of atoms from the layers of water for 1, 2 and 3 WL

```
> n[O[1,1]]:=v1;
n[O[2,1]]:=v2;   n[O[2,2]]:=v2;
n[O[3,1]]:=v3;   n[O[3,2]]:=v3;   n[O[3,3]]:=v3;
n[H[1,1]]:=2*v1;
n[H[2,1]]:=2*v2; n[H[2,2]]:=2*v2;
n[H[3,1]]:=2*v3; n[H[3,2]]:=2*v3; n[H[3,3]]:=2*v3;
```

$$n_{O_{1,1}} := 2$$

$$n_{O_{2,1}} := 2.7$$

$$n_{O_{2,2}} := 2.7$$

$$n_{O_{3,1}} := 2.7$$

$$n_{O_{3,2}} := 2.7$$

$$n_{O_{3,3}} := 2.7$$

$$n_{H_{1,1}} := 4$$

$$n_{H_{2,1}} := 5.4$$

$$n_{H_{2,2}} := 5.4$$

$$n_{H_{3,1}} := 5.4$$

$$n_{H_{3,2}} := 5.4$$

$$n_{H_{3,3}} := 5.4$$

The positions of the atoms in the clay platelet

```
> Z[O[0,1]]:=1.09;   Z[O[0,2]]:=3.28;   Z[F[0,1]]:=1.09;
Z[Li[0,1]]:=0.0;   Z[Mg[0,1]]:=0.0;   Z[Si[0,1]]:=2.70;
```

$$Z_{\mathrm{O}_{0,1}} := 1.09$$

$$Z_{\mathrm{O}_{0,2}} := 3.28$$

$$Z_{F_{0,1}} := 1.09$$

$$Z_{Li_{0,1}} := 0.$$

$$Z_{Mg_{0,1}} := 0.$$

$$Z_{\mathrm{Si}_{0,1}} := 2.70$$

The position of nickel ions for 0, 1, 2 and 3 WL

```
> Z[Ni[0,1]]:=5.70;
Z[Ni[1,1]]:=6.85;
Z[Ni[2,1]]:=7.95;
Z[Ni[3,1]]:=9.10;
```

$$Z_{Ni_{0,1}} := 5.70$$

$$Z_{Ni_{1,1}} := 6.85$$

$$Z_{Ni_{2,1}} := 7.95$$

$$Z_{Ni_{3,1}} := 9.10$$

The positions of the water molecules for 1, 2 and 3 WL

```
> Z[O[1,1]]:=6.85;
Z[O[2,1]]:=6.39;   Z[O[2,2]]:=6.39;
Z[O[3,1]]:=6.19;   Z[O[3,2]]:=6.19;   Z[O[3,3]]:=9.10;
Z[H[1,1]]:=6.85;
Z[H[2,1]]:=6.39; Z[H[2,2]]:=6.39;
Z[H[3,1]]:=6.19; Z[H[3,2]]:=6.19; Z[H[3,3]]:=9.10;
```

$$Z_{\mathrm{O}_{1,1}} := 6.85$$

$$Z_{\mathrm{O}_{2,1}} := 6.39$$

$$Z_{\mathrm{O}_{2,2}} := 6.39$$

$$Z_{\mathrm{O}_{3,1}} := 6.19$$

$$Z_{\mathrm{O}_{3,2}} := 6.19$$

$$Z_{O_{3,3}} := 9.10$$

$$Z_{H_{1,1}} := 6.85$$

$$Z_{H_{2,1}} := 6.39$$

$$Z_{H_{2,2}} := 6.39$$

$$Z_{H_{3,1}} := 6.19$$

$$Z_{H_{3,2}} := 6.19$$

$$Z_{H_{3,3}} := 9.10$$

G-factor from the atoms in the clay platelet. (minus oxygen)

```
>
G[ions]:=n[Li[0,1]]*f[Li]*cos(Z[Li[0,1]]*q)+n[F[0,1]]*f[F]*cos(Z[F[0,1]]*q)+n[Mg[0,1]]*f[Mg]*cos(Z[Mg[0,1]]*q)+n[Si[0,1]]*f[Si]*cos(Z[Si[0,1]]*q);
```

$$G_{ions} := 15.504 + 9.07 \cos(1.09\, q) + 28.58 \cos(2.70\, q)$$

```
>
G0[ions]:=n[Li[0,1]]*f[Li]+n[F[0,1]]*f[F]+n[Mg[0,1]]*f[Mg]+n[Si[0,1]]*f[Si];
```

$$G0_{ions} := 53.154$$

G-factor from oxygen in the clay platelet

```
>
G[O[0]]:=n[O[0,1]]*f[O]*cos(Z[O[0,1]]*q)+n[O[0,2]]*f[O]*cos(Z[O[0,2]]*q);
```

$$G_{O_0} := 16.10 \cos(1.09\, q) + 24.15 \cos(3.28\, q)$$

```
> G0[O[0]]:=n[O[0,1]]*f[O]+n[O[0,2]]*f[O];
```

$$G0_{O_0} := 40.25$$

G-factor for 1, 2 and 3 WL

```
> G[O[1]]:=G[O[0]] +
n[O[1,1]]*f[O]*cos(Z[O[1,1]]*q) +
n[H[1,1]]*f[H]*cos(Z[H[1,1]]*q);
```

$$G_{O_1} := 16.10 \cos(1.09\, q) + 24.15 \cos(3.28\, q) + 20.10 \cos(6.85\, q)$$

```
> G0[O[1]]:=G0[O[0]] +
n[O[1,1]]*f[O] + n[H[1,1]]*f[H];
```

$$G0_{O_1} := 60.35$$

```
> G[O[2]]:=G[O[0]] +
n[O[2,1]]*f[O]*cos(Z[O[2,1]]*q) +
n[H[2,1]]*f[H]*cos(Z[H[2,1]]*q)+
```

```
n[O[2,2]]*f[O]*cos(Z[O[2,2]]*q) +
n[H[2,2]]*f[H]*cos(Z[H[2,2]]*q);
```

$$G_{\mathrm{O}_2} := 16.10\cos(1.09\,q) + 24.15\cos(3.28\,q) + 16.100\cos(6.41\,q) + 2.0\cos(5.65\,q) + 2.0\cos(7.18\,q)$$

$$G_{\mathrm{O}_2} := 16.10\cos(1.09\,q) + 24.15\cos(3.28\,q) + 54.270\cos(6.39\,q)$$

```
> G0[O[2]]:=G0[O[0]] +
n[O[2,1]]*f[O] + n[H[2,1]]*f[H] +
n[O[2,2]]*f[O] + n[H[2,2]]*f[H];
```

$$G0_{\mathrm{O}_2} := 94.520$$

```
> G[O[3]]:=G[O[0]] +
n[O[3,1]]*f[O]*cos(Z[O[3,1]]*q) +
n[H[3,1]]*f[H]*cos(Z[H[3,1]]*q)+
n[O[3,2]]*f[O]*cos(Z[O[3,2]]*q) +
n[H[3,2]]*f[H]*cos(Z[H[3,2]]*q)+
n[O[3,3]]*f[O]*cos(Z[O[3,3]]*q) +
n[H[3,3]]*f[H]*cos(Z[H[3,3]]*q);
> G0[O[3]]:=G0[O[0]] +
n[O[3,1]]*f[O] + n[H[3,1]]*f[H]+
n[O[3,2]]*f[O] + n[H[3,2]]*f[H]+
n[O[3,3]]*f[O] + n[H[3,3]]*f[H];
```

$$G_{\mathrm{O}_3} := 16.10\cos(1.09\,q) + 24.15\cos(3.28\,q) + 54.270\cos(6.19\,q) + 27.135\cos(9.10\,q)$$

$$G0_{\mathrm{O}_3} := 121.655$$

Final G-factor for 0, 1, 2 and 3 WL

```
> G[L[0]]:=G[ions] + G[O[0]] +
n[Ni[0,1]]*f[Ni]*cos(Z[Ni[0,1]]*q);
```

$$G_{L_0} := 15.504 + 25.17\cos(1.09\,q) + 28.58\cos(2.70\,q) + 24.15\cos(3.28\,q) + 4.131000000\cos(5.70\,q)$$

```
> G[L[1]]:=G[ions] + G[O[1]] +
n[Ni[1,1]]*f[Ni]*cos(Z[Ni[1,1]]*q);
```

$$G_{L_1} := 15.504 + 25.17\cos(1.09\,q) + 28.58\cos(2.70\,q) + 24.15\cos(3.28\,q) + 24.23100000\cos(6.85\,q)$$

```
> G[L[2]]:=G[ions] + G[O[2]] +
n[Ni[2,1]]*f[Ni]*cos(Z[Ni[2,1]]*q);
```

$$G_{L_2} := 15.504 + 25.17\cos(1.09\,q) + 28.58\cos(2.70\,q) + 24.15\cos(3.28\,q) + 54.270\cos(6.39\,q) + 4.131000000\cos(7.95\,q)$$

```
> G[L[3]]:=G[ions] + G[O[3]] +
n[Ni[3,1]]*f[Ni]*cos(Z[Ni[3,1]]*q);
```

$$G_{L_3} := 15.504 + 25.17\cos(1.09\,q) + 28.58\cos(2.70\,q) + 24.15\cos(3.28\,q) + 54.270\cos(6.19\,q) + 31.26600000\cos(9.10\,q)$$

```
> G0[L[0]]:=G0[ions] + G0[O[0]] + n[Ni[0,1]]*f[Ni];
```

$$G0_{L_0} := 97.53500000$$

```
> G0[L[1]]:=G0[ions] + G0[O[1]] + n[Ni[1,1]]*f[Ni];
```

$$G0_{L_1} := 117.6350000$$

```
> G0[L[2]]:=G0[ions] + G0[O[2]] + n[Ni[2,1]]*f[Ni];
```

$$G0_{L_2} := 151.8050000$$

```
> G0[L[3]]:=G0[ions] + G0[O[3]] + n[Ni[3,1]]*f[Ni];
```

$$G0_{L_3} := 178.9400000$$

```
> IG[L[0]]:=(dw * G[L[0]]/G0[L[0]])^2;
```

$$IG_{L_0} := .0001051184681\,(\mathbf{e}^{(-.01000546688\,q^2)})^2\,(15.504 + 25.17\cos(1.09\,q) + 28.58\cos(2.70\,q) + 24.15\cos(3.28\,q) + 4.131000000\cos(5.70\,q))^2$$

```
> IG[L[1]]:=(dw * G[L[1]]/G0[L[1]])^2;
```

$$IG_{L_1} := .00007226481353\,(\mathbf{e}^{(-.01000546688\,q^2)})^2\,(15.504 + 25.17\cos(1.09\,q) + 28.58\cos(2.70\,q) + 24.15\cos(3.28\,q) + 24.23100000\cos(6.85\,q))^2$$

```
> IG[L[2]]:=(dw * G[L[2]]/G0[L[2]])^2;
```

$$IG_{L_2} := .00004339381646\,(\mathbf{e}^{(-.01000546688\,q^2)})^2\,(15.504 + 25.17\cos(1.09\,q) + 28.58\cos(2.70\,q) + 24.15\cos(3.28\,q) + 54.270\cos(6.39\,q) + 4.131000000\cos(7.95\,q))^2$$

```
> IG[L[3]]:=(dw * G[L[3]]/G0[L[3]])^2;
```

$$IG_{L_3} := .00003123094561\,(\mathbf{e}^{(-.01000546688\,q^2)})^2\,(15.504 + 25.17\cos(1.09\,q) + 28.58\cos(2.70\,q) + 24.15\cos(3.28\,q) + 54.270\cos(6.19\,q) + 31.26600000\cos(9.10\,q))^2$$

```
> 
plot({1*IG[L[0]],1*IG[L[1]],1*IG[L[2]],1*IG[L[3]]},q=0.2..4.00
,style=line);
```

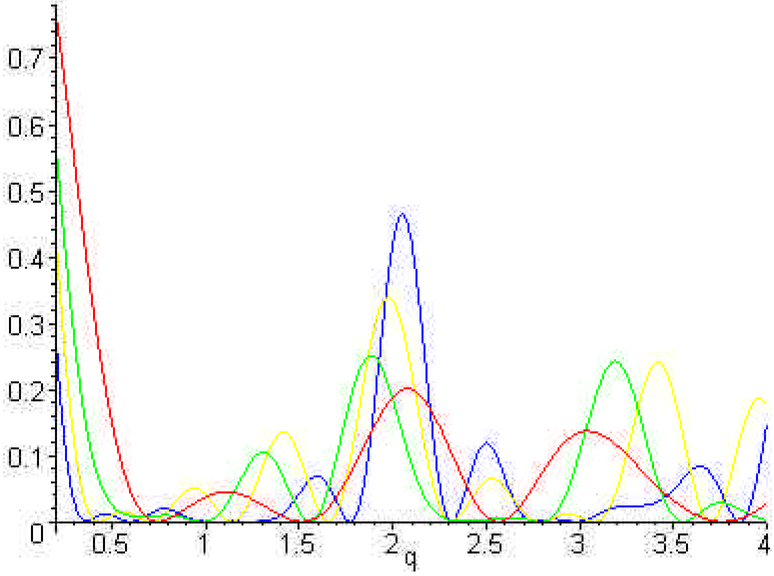

In this graph the red line is 0WL, green is 1WL, yellow is 2WL and blue is 3WL.

Explanation of the Maple-file

The values for v1, v2 and v3 were adjusted in the fittings used to find the n. The water is organised in 1, 2 and 3 layers, but this does not mean that there is 2 times as much water for 2WL than for 1WL. According to [14] neutron diffraction has shown that each interlayer nickel ion in vermiculite is coordinated octahedrally to 6.0 water molecules. But in addition to this, extra water is located to the clay layers. The amount of water in each layer is varied to make the best fits.

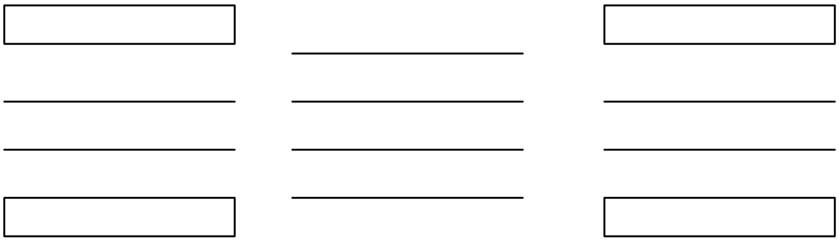

Figure F.1. Additional water is located to the clay layers, and the exact amount of water in each layer is unknown.

The atomic scattering factors, or structure factors, must be corrected for the temperature. The values follow the expression

$$f(t) = f(0) \cdot e^{-Wd \cdot \left(\frac{q}{4p}\right)^2} \qquad \text{(F.1)}$$

where Wd is the Debye-Waller factor, which is dependent on the temperature. According to [15] the values for cations are 1.4 and for oxygens 1.8. In an X-ray study [5] they have used a single mean value for the Debye-Waller factor. We have done the same simplifying in our calculations. Even though this temperature correction is dependent on q it does not interfere too much on our calculations, but it is carried on to make them more rigorous.

According to [4] the layer charge for fluorohectorite is 1.2e$^-$ pr Si_8O_{20} unit. We only use half of this unit formula, we only look at half of the unit cell because of symmetry and Ni is 2+, so this gives 0.15 as the number of Ni^{2+}-ions, or half the value for Li^+. Because of the symmetry we position the water molecules for two layers at only one position and for three layers at the centre position plus two times the position below the centre in figure 4.15.

The graph on the previous page shows the simulated G^2 for the different water layers.

Appendix G

Functions to be fitted in Origin

This appendix contains the functions that were used to fit the peak values for the clean water layers to find the best value for n for our clay samples. TK is thick sample or the sample used for bulk scattering, while TN is the thin surface scattering sample. IG is G^2.

TK 0WL

$$IG_{L_0} := \left(\mathbf{e}^{(-.01000546688 q^2)}\right)^2 (-9.17\, nLi + 25.17 \cos(1.09\, q) + 18.255 + 28.58 \cos(2.70\, q) + 24.15 \cos(3.28\, q) + 13.77000000\, nLi \cos(5.70\, q))^2 \big/ (4.60000000\, nLi + 96.155)^2$$

peak	xc	value (top-background)
001	0.550	0.01025
002	1.100	0.00109
004	2.200	0.0007925
005	2.750	0.0004096

Function to fit in Origin:

```
G1=exp(-0.01*x^2)^2
G2=-9.17*nLI+25.17*cos(1.09*x)+18.255+28.58*cos(2.7*x)
G3=24.15*cos(3.28*x)+13.77*nLI*cos(5.7*x)
G4=4.6*nLI+96.155
G=G1*(G2+G3)^2/G4^2

Q=0.09522*x
num=1-2Q^2+2Q^4
den=(1-Q^2)*Q^(n+1)
lf=num/den

y=y0+Amp*G*lf
```

TK & TN 1WL

$$IG_{L_1} := \left(\mathbf{e}^{(-.01000546688 q^2)}\right)^2 (-9.17\, nLi + 25.17 \cos(1.09\, q) + 18.255 + 28.58 \cos(2.70\, q) + 24.15 \cos(3.28\, q) + 10.05\, v1 \cos(6.85\, q) + 13.77000000\, nLi \cos(6.85\, q))^2 \big/ (4.60000000\, nLi + 96.155 + 10.05\, v1)^2$$

```
G1=exp(-0.01*x^2)^2
G2=-9.17*nLI+25.17*cos(1.09*x)+18.255+28.58*cos(2.7*x)
G3=24.15*cos(3.28*x)+10.05*v1*cos(6.85*x)+13.77*nLI*cos(6.85*x)
G4=4.6*nLI+96.155+10.05*v1
G=G1*(G2+G3)^2/G4^2
```

```
Q=0.09522*x
num=1-2Q^2+2Q^4
den=(1-Q^2)*Q^(n+1)
lf=num/den

y=y0+Amp*G*lf
```

TKTN 2WL

TN2WL is not stable, and these values are not included.

$$IG_{L_2} := \left(\mathbf{e}^{(-.01000546688\, q^2)}\right)^2 (-9.17\, nLi + 25.17 \cos(1.09\, q) + 18.255 + 28.58 \cos(2.70\, q) + 24.15 \cos(3.28\, q) + 20.10\, v2 \cos(6.39\, q) + 13.77000000\, nLi \cos(7.95\, q))^2 \Big/ (4.60000000\, nLi + 96.155 + 20.10\, v2)^2$$

```
G1=exp(-0.01*x^2)^2
G2=-9.17*nLI+25.17*cos(1.09*x)+18.255+28.58*cos(2.7*x)
G3=24.15*cos(3.28*x)+20.10*v2*cos(6.39*x)+13.77*nLI*cos(7.95*x)
G4=4.6*nLI+96.155+20.10*v2
G=G1*(G2+G3)^2/G4^2

Q=0.09522*x
num=1-2Q^2+2Q^4
den=(1-Q^2)*Q^(n+1)
lf=num/den

y=y0+Amp*G*lf
```

TKTN 3WL

$$IG_{L_3} := \left(\mathbf{e}^{(-.01000546688\, q^2)}\right)^2 (-9.17\, nLi + 25.17 \cos(1.09\, q) + 18.255 + 28.58 \cos(2.70\, q) + 24.15 \cos(3.28\, q) + 20.10\, v3 \cos(6.19\, q) + 10.05\, v3 \cos(9.10\, q) + 13.77000000\, nLi \cos(9.10\, q))^2 \Big/ (4.60000000\, nLi + 96.155 + 30.15\, v3)^2$$

```
G1=exp(-0.01*x^2)^2
G2=-9.17*nLI+25.17*cos(1.09*x)+18.255+28.58*cos(2.7*x)
G3=24.15*cos(3.28*x)+20.10*v3*cos(6.19*x)+10.05*v3*cos(9.1*x)+13.77*nLI*cos(9.1*x)
G4=4.6*nLI+96.155+30.15*v3
G=G1*(G2+G3)^2/G4^2

Q=0.09522*x
num=1-2Q^2+2Q^4
den=(1-Q^2)*Q^(n+1)
lf=num/den

y=y0+Amp*G*lf
```

Appendix H

The Maple-file used to calculate the impact of slit size on peak shapes

```
>  restart;
```

Width of Lorenz peak

```
> wl:=0.01;
```

$$wl := .01$$

```
> L:=x -> 1/(4*x^2+wl^2);
```

$$L := x \rightarrow \frac{1}{4\,x^2 + wl^2}$$

Width of detector slits (0.004Å-1 given by the width of the quartz peak)

```
> ws:=0.004;
```

$$ws := .004$$

```
> func:=int(L(x),x=q-ws..q+ws);
```

$$func := 50.\ \arctan(200.\ q + .800) - 50.\ \arctan(200.\ q - .800)$$

```
> with(student);
```

$$[D, Diff, Doubleint, Int, Limit, Lineint, Product, Sum, Tripleint, changevar, completesquare, distance, equate, integrand, intercept, intparts, leftbox, leftsum, makeproc, middlebox, middlesum, midpoint, powsubs, rightbox, rightsum, showtangent, simpson, slope, summand, trapezoid]$$

```
> func:=makeproc(func,q);
```

$$func := q \rightarrow 50.\ \arctan(200.\ q + .800) - 50.\ \arctan(200.\ q - .800)$$

Must divide with a factor so the top points are at equal height

```
> div:=L(0)/func(0);
```

$$div := 148.2050277$$

```
> plot({func(q),L(q)/div},q=-0.03..0.03);
```

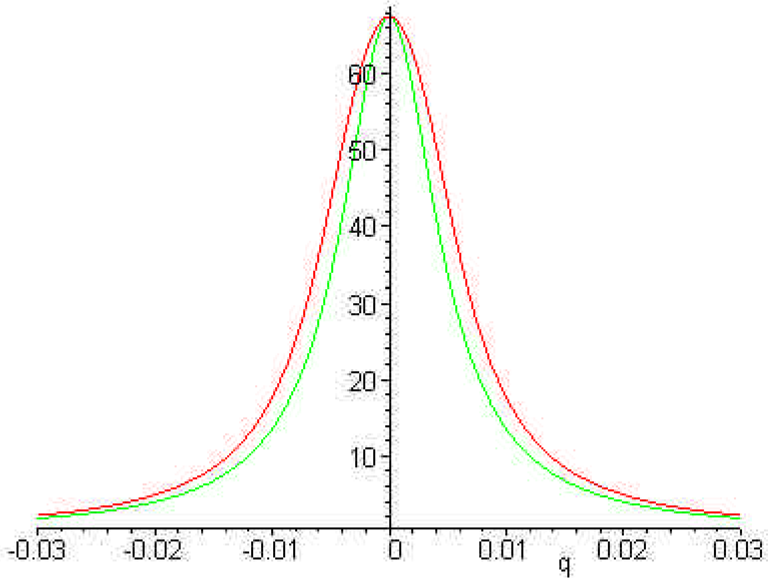

REFERENCES

[1] B. Velde, *Introduction to Clay Minerals - Chemistry, Origins, Uses and Environmental Significance.* Chapman & Hall, 1992.

[2] H. van Olphen, *An introduction to Clay Colloid Chemistry - Second edition.* Krieger Publishing Company, Malabar, Florida, 1991.

[3] Jean-Cristophe P. Gabriel et al. *Observation of Nematic Liquid-Crystal Textures in Aqueous Gels of Smectite Clays.* J. Phys. Chem. 1996, 100, 11139-43. American Chemical Society.

[4] P.D. Kaviratna et al. *Dielectric Properties of Smectite Clays.* J. Phys. Chem. Solids, Vol. 57, No. 12, 1996, 1897-1906.

[5] S. Lee & S.A. Solin. *X-ray study of the intercalant distribution in mixed alkyl ammonium pillared clay.* Physical Review B, Volume 43, Number 14, 1991.

[6] Jacob Israelacivili. *Intermolecular & Surface Forces - Second Edition.* Academic Press Limited, 1992.

[7] Mikkelsen, Elgeseter & Stokke. *Molecular Biophysics.* NOBIPOLs research foundation, Trondheim, Norway.

[8] H.P. Klug & L.E. Alexander. *X-ray Diffraction Procedures - Second Edition.* John Wiley & Sons, New York.

[9] Duane M. More & Robert C. Reynolds Jr. *X-ray Diffraction and the Identification and Analysis of Clay Minerals.* Second edition. Oxford University Press, 1989.

[10] G.K. Williamson & W.H. Hall. *X-ray Line Broadening from Filed Aluminium and Wolfram.* Acta Metallurgica, Vol. 1, 1953.

[11] C. Hammond. *The Basics of Crystallography and Diffraction.* Oxford Science Publications, 1997.

[12] N.T. Skipper, K. Refson, J.D.C. McDonnel. *Computer Simulation of Interlayer Water in 2:1 Clays.*.Journal of Chemical Physics, 94, 7434-7445 (1991).

[13] S. Karaborni et al. *The Swelling of Clays: Molecular Simulations of the Hydration of Montmorillonite.* Science, Vol. 271, P.1102-04.

[14] N.T. Skipper et al. *The Structure of Interlayer Water in Vermiculite.* Journal of Chemical Physics, 94, 5751-5760 (1991).

[15] G.W. Brandly & G. Brown. *Crystal Structures of Clay Minerals and their X-ray Identification.* Mineralogical Society, London, 1980.

[16] S.B. Lutnæs, *Experimental Studies of Water Intercalation in a Layered Silicate System.* Diploma thesis, NUST, 1999.

[17] Supervisor Dr.ing. Jon Otto Fossum’s web page.
http://www.phys.ntnu.no/~fossumj/